國 立 交 通 大 學
電機與控制工程研究所
碩士論文

微型陀螺儀的強健控制器設計

Design of Robust Controller for Micro
Vibratory Ring Gyroscope

研究生：楊昇儒

指導教授：邱一 博士

中華民國九十七年十月

微型陀螺儀的強健控制器設計

Design of Robust Controller for Micro Vibratory Ring Gyroscope

研 究 生: 楊昇儒   Student: S. R. Yang

指導教授: 邱一   Advisor: Yi Chiu

國立交通大學 電機學院

電機與控制工程研究所

碩士論文

A Thesis
Submitted to Department of Electrical and Control Engineering
College of Electrical Engineering
National Chiao Tung University
In Partial Fulfillment of the Requirement
For the Degree of
Master
In

Electrical and Control Engineering

October 2008

Hsinchu, Taiwan, R.O. C

中華民國九十七年十月

中文摘要

　　隨著微機電科技的進步，微型陀螺儀的應用日益廣泛，如在汽車的導航及安全控制、遊戲主機、手機等都可發現其蹤跡。對於目前的微機電式陀螺儀而言，製造過程中的誤差及使用過程中的磨損會造成成品與設計間存在差異，以至於無法滿足原先系統的規格。本研究的重點在於設計一控制器，能在微型陀螺儀的特性參數發生變異時，還能保有一定的系統性能。

　　因為陀螺儀本身屬於多輸入多輸出系統 (multi-input multi-output, MIMO)，且驅動軸與感測軸間有耦合的情形，若系統特性有變異時，無法利用一般的 PID 控制設計方法來達成規格要求。因此，我們必須設計一個既可以控制 MIMO 系統又可以忍受特性參數變異的穩健控制器(robust controller)。在此論文中我們會先忽略系統變異並利用 pole placement 的控制理論設計出 PID 控制器，之後再利用穩健控制理論中的 H_∞ 理論結合量化迴授理論(quantitative feedback theory, QFT)設計出穩健控制器，最後比較不同控制器的性能和穩健特性等差異。

　　論文中，我們先找出受控體的特性矩陣 P(s)和權重函數，並使用 MATLAB 輔助完成控制器的設計。當系統的共振頻率和阻尼係數存在 10%變異量時，加入 PID 控制的系統響應變異量為 24%，而加入 QFT/H_∞控制器的變異量為 5.6%，且暫態響應的特性仍能符合規格，包含安定時間小於 0.2ms，最大超越量低於10%，可知利用 QFT/H_∞的控制方法設計出的控制器在穩健性上有明顯的改善。此外和一般 H_∞控制器相比，系統迴路由狀態回授變為輸出回授，因而在實現上也較為容易。

Abstract

With the progress of the MEMS technology, the application of micro-gyroscopes becomes more and more extensive. Examples can be found in automobile navigation and safety control, game hosts, mobile phones, etc.. However, fabrication errors and operation wearout will cause difference in component characteristics between the expected value and the actual value in real devices. The objective of this research is focused on the design of a controller which can maintain certain system performance in the presence of the system characteristic parameter variation.

The gyroscope is a multi-input multi-output (MIMO) system with possible variations in system characteristics. Therefore, the common PID controller design method can not be used in controller design to meet the specification. A robust controller which can be used to control a MIMO system and endure parameter variation is required. In this thesis, the pole placement method is applied to design a PID controller without considering the system variation. Then the H_∞ theory and quantitative feedback theory (QFT) are applied to design the controller. The performance and the robustness of the controllers are compared.

After determining the characteristic matrix P of the plant and the weighting functions, the controller is calculated by MATLAB. When the natural frequency and the damping coefficient both have variation of 10%, the variation of the system response is 5.6% in QFT/H_∞ controller and 24% in PID controller. Therefore, the QFT/H_∞ control method has better robustness. Compared with conventional H_∞ controller, the QFT/H_∞ control loop uses output feedback and is easier to realize.

致謝

　　兩年的碩士班生涯即將結束，這段時間對我而言是人生中不可缺乏的階段，我感到獲益良多。首先要謝謝我的指導教授邱一老師，他總是給我許多專業的意見和方向，也教導了我正確的學習態度以及研究精神，且不厭其煩的給我指導，使我在他身上學到許多，在此要真心的感謝老師，「老師！您辛苦了！」此外要謝謝我的口試委員，邱俊誠博士和蕭得聖博士，謝謝您們給我的種種意見，讓我發現許多考慮不周詳的地方。

　　兩年的時間，有辛苦也有歡樂，這都要感謝實驗室的成員們。感謝實驗室的學長：忠衛、炯廷、建勳、均宏、亦謙、繁果和煒智，謝謝你們這段時間來傳授我許多實驗上的經驗和知識；感謝陪伴我兩年和我一起努力的同學：子麟、弘諳、昌修，這段時間咱們互相勉勵互相扶持，我不會忘記你們的，期望以後畢業後仍有相聚的機會；感謝帶給我歡樂的學弟妹：建安、經富、鴻智、政安、俊宏、姿穎、哲明，在接近畢業的時候，許多雜事都落到了你們身上，辛苦你們了。接著要感謝我的父母和家人，因為有你們幫忙，讓我不愁吃穿，且在我遇到困難和失落時，給我支持和鼓勵。特別要感謝的是我的女友慧萱，感謝妳這段時間給我的鼓勵和幫助，妳是讓我支持下去的最重要因素，謝謝妳！

　　最後，謝謝曾經幫助過我的人，畢業之後就要離開校園踏入職場，期許自己能將這兩年的所學經驗，充分運用在之後的日子，為社會盡我微薄之力。

楊昇儒 謹識

中華民國九十七年十月

新竹 交大

Table of Content

List of Figures

List of Tables

Chapter 1   Introduction

Gyroscopes are used to measure the angular rate in vehicle navigation, guidance, rollover stability, and in aerospace applications such as aircrafts and satellites. Therefore, the accuracy and precision of gyroscopes have been the targets of intensive studies. Gyroscopes have been developed for a long time, but traditional gyroscopes are too big and expensive. Therefore, MEMS gyroscopes are becoming more popular in electronic and consumer market.

Micro Electro-Mechanical Systems (MEMS) have the advantages of small dimensions, mass production, and integration with electronic circuits. It has been used in various sensing applications, such as pressure sensors, temperature sensors, radiation sensors, and inertial sensors such as accelerometers and gyroscopes. Another advantage is that MEMS devices can be fabricated with electric circuits on a single chip. Therefore, low cost and high performance system can be achieved.

For MEMS gyroscopes, accuracy, stability, and robustness are important performance characteristics. Fabrication deviations and operation wear-out are typical reasons for the variation and non-ideality of system characteristics variation and quadrature error. Post-fabrication trimming can be used to adjust the device parameters with high cost [1]. In order to maintain wide fabrication process windows and long-term stability, MEMS gyroscopes can also be operated with an active feedback control to compensate for these deviations. Complex control algorithms such as adaptive control [2, 3], H_∞ control [4], automatic gain control [5, 6] and active disturbance rejection control [5] have been reported in the literature. However, complex systems are not necessarily the best solutions for commercialization. In this thesis, the QFT/H_∞ control method will be studied. The performance of various

control systems will be compared when the system characteristic parameters have variation.

1.1 Gyroscope

The development of the gyroscope can be traced back to 1852 when the French experimental physicist Leon Foucault used an equipment called "gyroscope" to study the rotation of earth. Since then, gyroscopes have been used for measuring angular rate in many navigation, homing, and stabilization applications. Many different gyroscopes have been developed.

The gyroscope is a two degrees of freedom (2-DOF) mass-spring-damper system. When there is an angular rate acting on the gyroscope, the sense axis of the gyroscope is affected by the Coriolis force. The force is proportional to the angular rate and measured as the output of the gyroscope. Although conventional rotating wheel gyroscopes have dominated high-precision applications, they are large and most often too expensive to be used in many applications [3]. On the other hand, sensitivity, reliability and the miniaturization of mass producible gyroscopes are more and more important for consumer applications.

1.1.1 MEMS gyroscope

A MEMS gyroscope is an angular rate sensor whose size is much smaller than most mechanical gyroscopes. In batch fabrication, hundreds of MEMS gyroscopes can be produced in a wafer. Fig. 1.1 shows an example of a bulk-micromachined gyroscope [6]. Compared with mechanical gyroscopes, MEMS gyroscopes are much smaller and inexpensive.
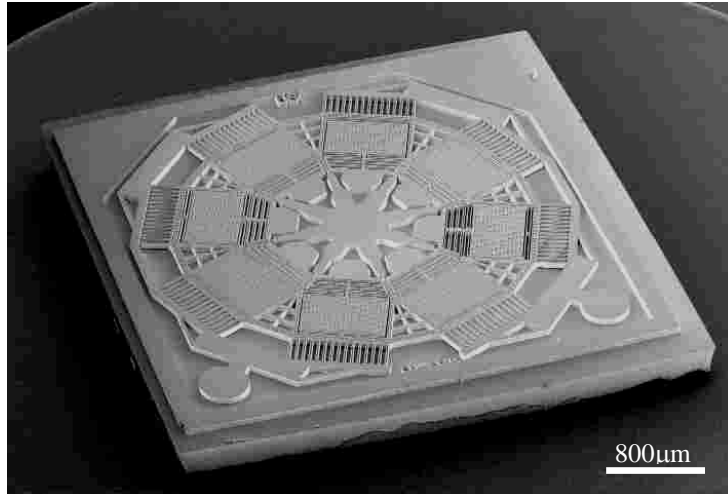
Fig. 1.1 A prototype bulk-micromachined gyroscope, diced and released [6]

The reported micromachined gyroscopes almost all use vibrating mechanical elements to sense the angular rate. Because the silicon material has fine mechanical characteristics, the MEMS vibratory gyroscopes are almost all fabricated in silicon substrates. The main advantage of semiconductor silicon fabrication process is matured technology that is suitable for mass production. The other MEMS fabrication process, like LIGA [7], LIGA-like [8], and SOI wafer fabrication process [9] are also applied to gyroscope fabrication. Various types of MEMS gyroscopes are reviewed in the following.

1.1.2 Vibrating beam gyroscope

A simple vibrating beam gyroscope is shown in Fig. 1.2 [10]. There is a rectangle ditch which is chromium-plated at the bottom of the glass substrate as a sense electrode of the *x*-axis under the vibrating beam. A piezoelectric vibrator drives the beam in the *y*-axis. In the presence of a *z*-axis rotation, the *x*-axis will vibrate due to the Coriolis force. This structure uses capacitance change to calculate the angular rate.
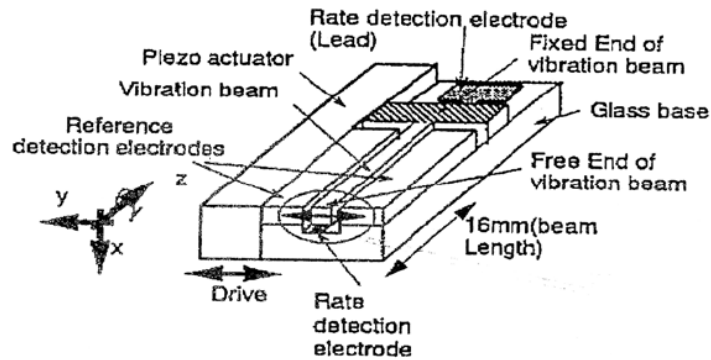
Fig. 1.2 Vibrating beam gyroscope [10]

1.1.3 Tuning fork gyroscope

Tuning fork gyroscopes [11, 12] have been used for many years. A micro machined tuning fork gyroscope is shown in Fig. 1.3. The principle of the tuning fork gyroscope is similar to the principle of the vibrating beam gyroscope. There is no net torque at the junction and stable conditions can be obtained for the balanced system with two bars oscillating oppositely. It leads to low energy loss and high Q factor.

The tuning fork is driven by the tuning/balance electrodes with a phase difference of 180°. When there is an angular rate in vertical direction, the Coriolis force causes torsion of the tuning fork. The torsion can be sensed by the sense electrodes and the angular rate can be derived.
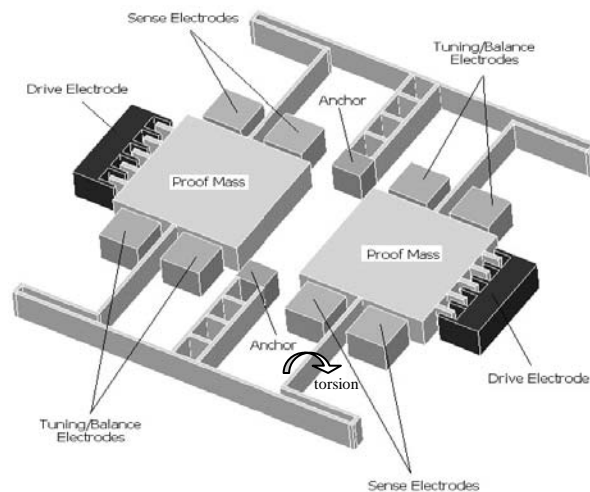
Fig. 1.3 Tuning fork MEMS gyroscope [11]

1.1.4 Vibrating ring gyroscope

A vibrating ring gyroscope is shown in Fig. 1.4 [12]. A sustaining cylinder suspends the ring structure in the center of the device. The ring structure can be electrostatically actuated and capacitively sensed by the surrounding electrodes. The ring is connected to the center axis by eight semicircular springs. When the ring structure is actuated by applying a voltage to the driving electrodes, the Coriolis force will cause the ring to vibrate in the direction of $45°$ from the driving axis. The angular rate is derived from the capacitance sensing electrodes.
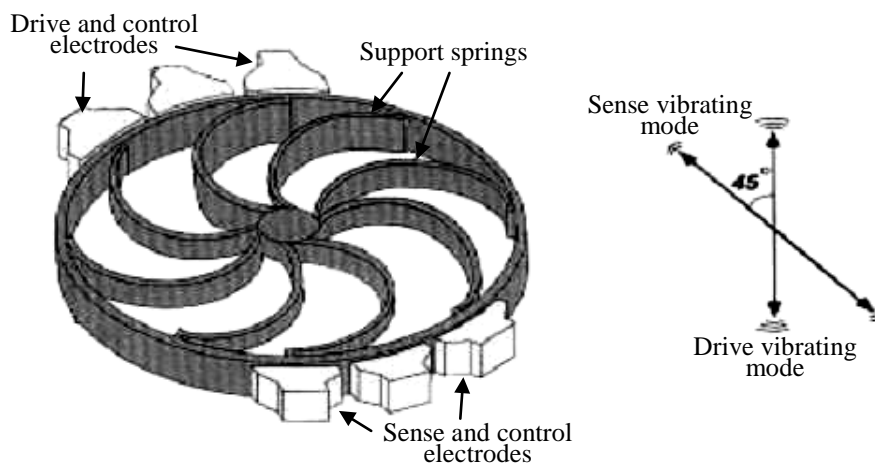
Fig. 1.4 Vibrating ring gyroscope [12]

1.1.5 Frame gyroscope

Fig. 1.5 shows the inside drive outside sense (IDOS) and inside sense outside drive (ISOD) frame gyroscopes, respectively [13]. In both devices, there is an inner mass connected via mechanical springs to the outer frame that is anchored to the substrate via another set of springs. The design of the springs is such that the two masses are compliant in two orthogonal directions, namely the drive (x-axis) and sense (y-axis) directions. Since the drive resonant motion is typically much larger than

the sense motion, the lateral comb finger drive is used for driving the structures while parallel-plate sense combs are used to sense the Coriolis force.

For the Type A device, the inner mass (drive mass) is driven into resonance by applying sinusoidal voltages to the lateral combs using an on-chip closed-loop drive circuitry. In the presence of z-axis rotation rate, Coriolis force acts along y-axis on the oscillating drive mass. The change in capacitance arising from this sense motion yields an output proportional to the input rotation rate.

For the Type B device, the driving force is applied to the outer frame (drive mass) which causes both the mass to oscillate along the drive axis. In response to a z-axis angular rate, Coriolis force acts on both masses. However, only the sense mass responds to Coriolis force due to stiff drive springs along the sense axis.
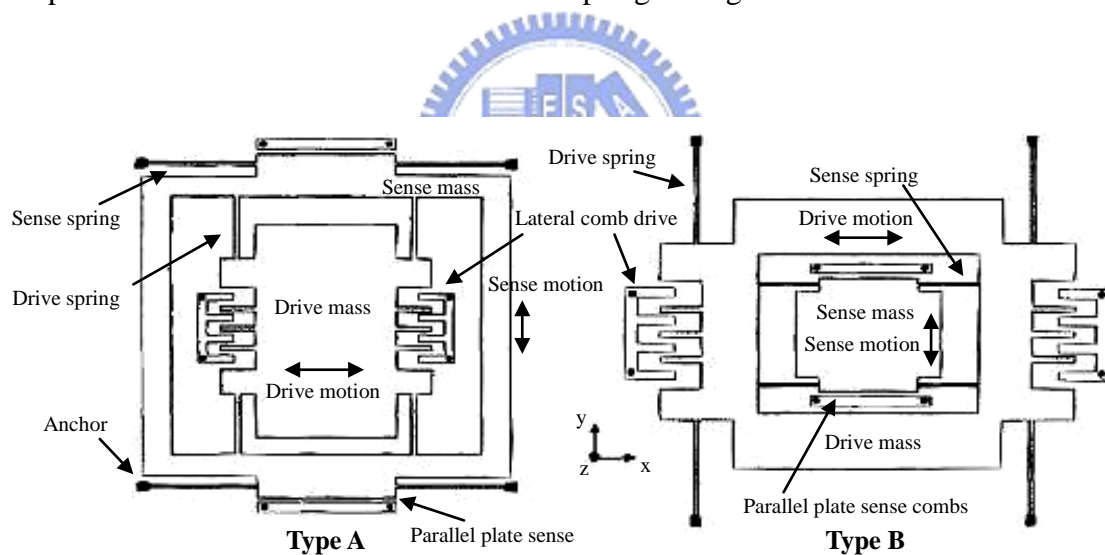
Fig. 1.5 Frame gyroscope [13]

1.2 Gyroscope control

Various control methods have been applied to control MEMS gyroscopes. In this section, some common MEMS gyroscope control methods are reviewed.

1.2.1 Adaptive control

Adaptive control is a useful method for the operation of MEMS z-axis

gyroscopes [2, 3]. The proposed control scheme estimates the component of the angular rate orthogonal to the plane of oscillation of the gyroscope. The control loop is composed of a band-pass filter, a parameter adaptation algorithm and a modulation, as shown in Fig. 1.6 [14]. The parameter adaptation algorithm (PAA) block in Fig. 1.6 estimates the angular rate, identifies and compensates the quadrature error, and may permit on-line automatic mode tuning. Its goal is to achieve compensation of fabrication imperfections, closed-loop estimation of the angular rate, to attain a large bandwidth and dynamic range, and self-calibration operation.
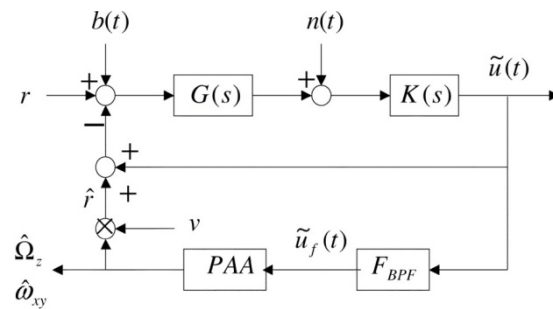
Fig. 1.6 Block diagram of the adaptive add-on control [14]

1.2.2 H$_\infty$ control

Since the MEMS gyroscope is operated at its resonant frequency, its high quality factor limits its bandwidth under an open loop condition. To improve the bandwidth of the gyroscope, an H$_\infty$ controller was proposed and developed in [4]. The analysis and test results showed that the proposed controller enlarged the bandwidth and enhanced the linearity. It was also shown that the H$_\infty$ controller was more robust compared with traditional control methods such as the PID controller.

In order to design the H$_\infty$ controller, the plant model in Fig. 1.7 (a) should be transformed into a two-port system illustrated in Fig. 1.7 (b).The H$_\infty$ control problem is to find a controller which makes the infinity norm of the transfer function from w to

z minimum, where *w* is a signal including noises, disturbances, and reference signals, *z* is a signal including all controlled signals and tracking errors. Because *z* is composed of output and control input, the H$_\infty$ controller minimizes the output and the control input for the external angular rate, which is indispensable to achieve the wide bandwidth and dynamic range.
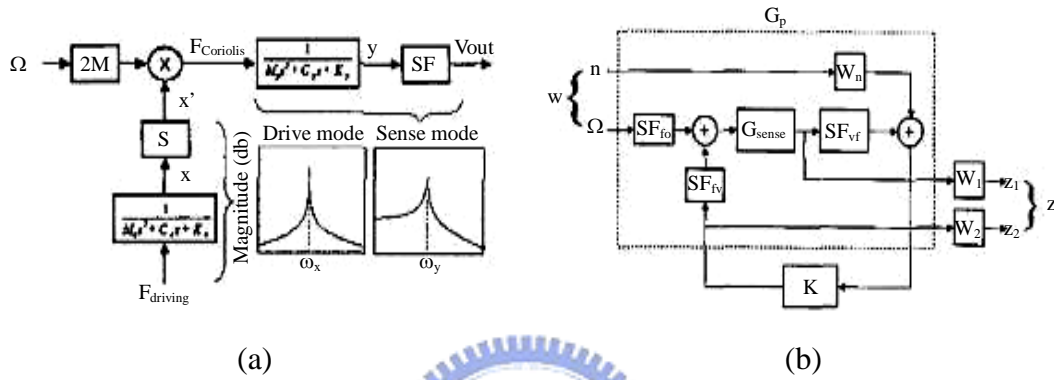
Fig. 1.7 (a) Plant model, (b) block diagram of MEMS gyroscope with H$_\infty$ controller [4]

1.2.3 AGC force rebalance control

Force rebalance control can be applied via the automatic gain control (AGC) method [15, 16]. The rebalance control design takes advantages of AGC loop modification, which allows the approximation of the system dynamics into a simple linear form. Using the AGC and the rebalance control that maintains a biased oscillation, bandwidth and operating range can be improved.

Fig. 1.8 (a) shows the proposed feedback system which is a modification from the normal AGC loop design. In the figure, *u* denotes a controller output, u_m denotes a modulated control signal, ω_y denotes a natural frequency, and ζ_y denotes a damping ratio, respectively. Note that the plant output *z* implies the velocity signal and the output of the low pass filter *y* is its scaled envelope signal. The block diagram in Fig. 1.8 (b) shows the practical implementation of the vibratory MEMS gyroscope and the

electronics for signal processing and control. In the figure, the lower loop is implemented for the force rebalance and the upper loop is for the lateral oscillation in the driving mode dynamics. The rebalance loop is implemented through the combination of a charge amplifier, analog differentiator, and demodulator for envelope detector, controller, voltage gain and analog multiplier.

(a)   (b)
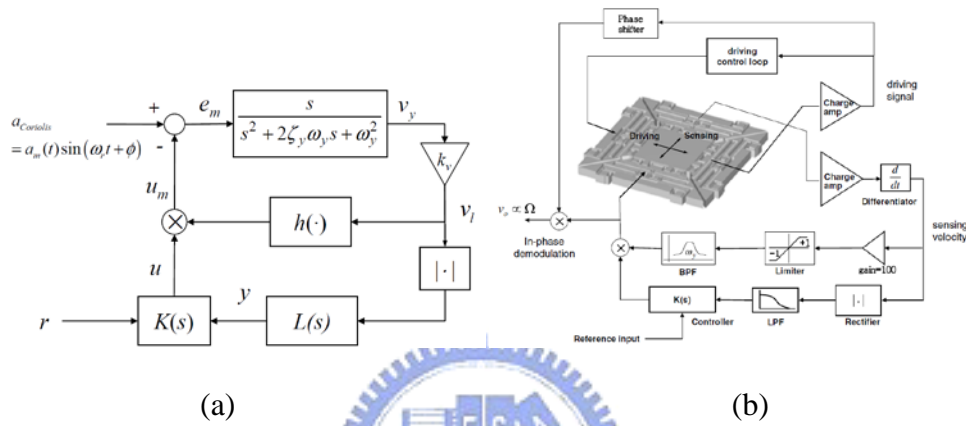
Fig. 1.8 (a) Force rebalance configuration with a modified AGC loop, (b) block diagram and electronics for force rebalance [16]

1.2.4 Active disturbance rejection control

Another control solution of the MEMS gyroscopes is the active disturbance rejection control (ADRC) [5]. This control method can solve the problem of mismatched natural frequencies of the two axes in a vibrating MEMS gyroscope. It can also solve the problems of the mechanical-thermal noise, the quadrature errors, and the parameter variations. The extended state observer (ESO) is applied to the feedback control. Then the controller drives the drive axis to the desired trajectory and forces the vibration of the sense axis to be zero by force rebalance. Thus, the angular rate can be estimated precisely by the demodulator.

The estimation of the angular rate is based on the accurate state estimation and the good tracking of the drive axis and the sense axis. The block diagram of ADRC is

shown in Fig. 1.9. In the figure, the ESO provides an estimate of the external disturbances and plant dynamics, and the demodulation block is applied to estimate the angular rate.
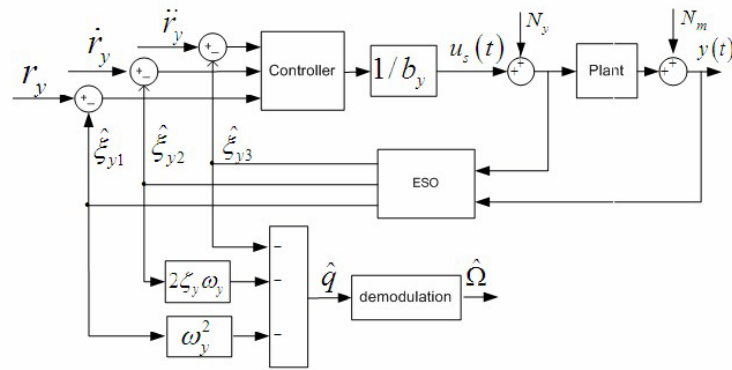
Fig. 1.9 Block diagram of the ADRC and rate estimation [5]

1.2.5 Summary

The above control methods have their advantages and disadvantages. Because the assumptions and specifications of the controllers are different, it is difficult to compare the performance fairly.

Adaptive control is the most widely-used method in MEMS gyroscope control. But the multiple tuning parameters of the controller make it difficult to realize in real world. H_∞ control is a good method for robustness. But in [4], the quadrature error and the effect on the drive axis by the displacement of the sense axis were ignored. The disadvantage of AGC force rebalance control is that double-tuned high-Q filters are required to prevent the signals from interfering with the detectors. The disadvantages of ADRC control are that it is complicated and has an inherent assumption that the disturbance is already given. Therefore, a robust controller designed by QFT/H_∞ control method is studied in this thesis.

1.3 Objectives and thesis organization

The objective of this thesis is to design a controller to maintain the system performance when the characteristic parameters have variation. First, the PID control design using pole placement is presented. Then the QFT/H$_\infty$ theory is applied to design a robust controller [17]. The performance of the PID control, QFT/H$_\infty$ control and the results from other publications are also compared.

In this thesis, the analysis of the micro vibrating ring gyroscope is given in Chapter 2. The controller design is discussed in Chapter 3. The simulation and comparison of the different controllers applied to the MEMS gyroscope are presented in Chapter 4. Finally, conclusion and future work are discussed in Chapter 5.

Chapter 2 Principle of MEMS gyroscope

The overview of the micro vibrating ring gyroscope to be studied in this thesis is shown in Fig. 2.1. The design of this device is provided by Chung-Shan Institute of Science.

The main sense component is a suspended ring supported by elastic suspension structures. The structure thickness is the thickness of the silicon substrate. There are electrodes of drive, sense, and control. Electrostatic forces are applied to drive and control the device. The ring is driven along the drive axis at the resonant frequency. The angular rate Ω is measured by detecting the capacitance change due to the gap variation along the sense axis. A feedback force is used to counteract the Coriolis force caused by the rotation, thus maintaining the amplitude of the sense mode at zero.
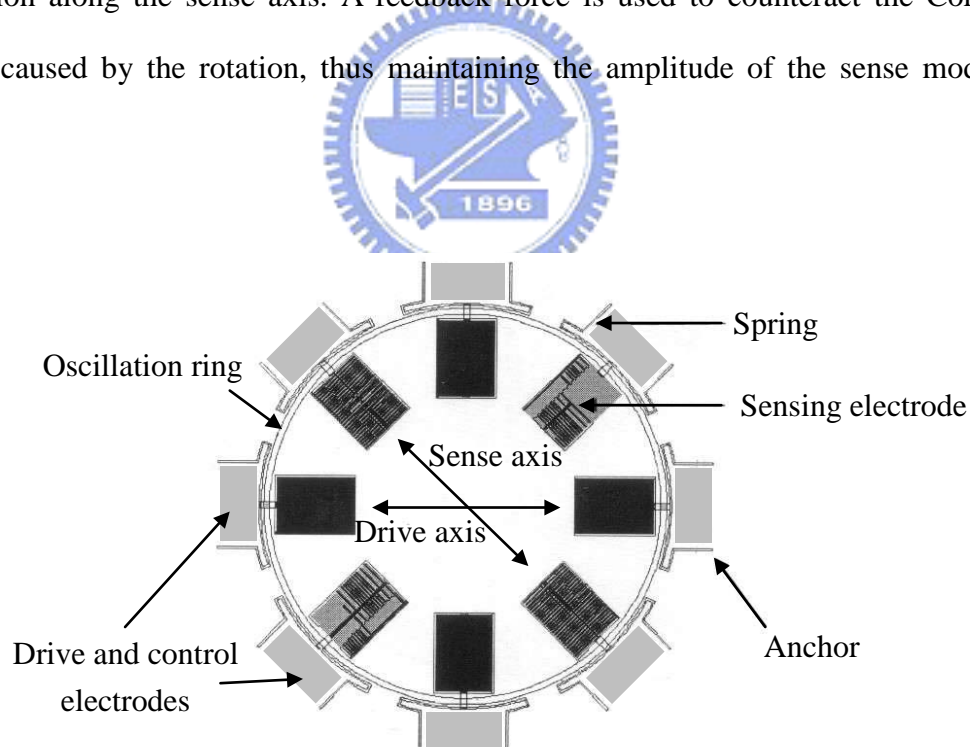
Fig. 2.1 Overview of the micro vibrating ring gyroscope

Coriolis acceleration, as illustrated in Fig. 2.2, is an apparent deflection of moving objects when they are viewed from a rotating reference frame [18]. If the

coordinate system along with the observer starts rotating around the *z*-axis with an angular rate Ω, the observer thinks that the trajectory of the object deflects toward the *y*-axis with the acceleration equal to 2*v*Ω where *v* is the velocity of the object as measured in the rotating reference frame. Although no real force has been acted on the object, to an observer who is attached to the rotating reference frame, an apparent force has arisen that is directly proportional to the rate of rotation Ω. This Coriolis effect is the basic operating principle of gyroscopes.
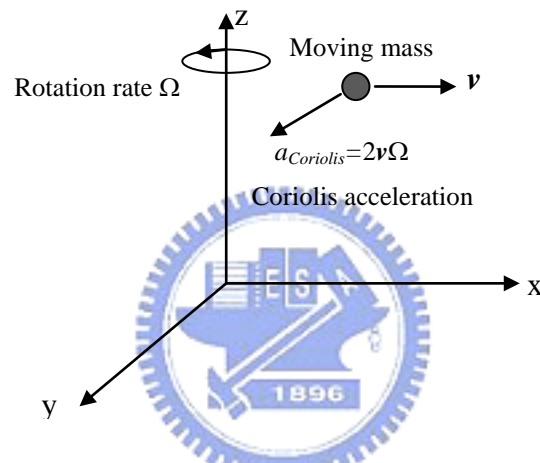
Fig. 2.2 Concept of the Coriolis acceleration

The Coriolis acceleration is given by the vector cross product of the angular rate Ω and the velocity of the object *v*. In Fig. 2.2, the velocity is oriented along the *x*-axis and the Coriolis acceleration is along the *y*-axis. Therefore, a gyroscope in this configuration can detect the angular rate of the *z*-axis by measuring the deflected trajectory in the *y*-axis (sense axis).

2.1 Operating principle

In a vibrating ring gyroscope, energy is transferred between two vibration modes due to the action of the Coriolis acceleration. Since the Coriolis force is proportional

to the rate of rotation Ω. The angular rate can be determined by sensing the Coriolis-induced vibration.

In an ideal vibrating ring gyroscope, the ring structure has two degenerate fundamental resonance modes which are shown in Fig. 2.3. These modes can be excited by appropriate driving signal. General MEMS gyroscopes are often driven by electrostatic force. The resonance of the drive mode has maximum amplitude at 0°and 90° direction, and nodes A at the 45° direction. The long axis and short axis of the elliptic mode shape does not rotate when the angular rate is zero; therefore the position of the node does not move. If a displacement sensor is placed at the node position, the output is zero. Nevertheless, if there is an angular rate, the Coriolis force will make the axes of the mode shape rotate. We can regard this as the coupling of the drive mode and the sense mode under the effect of Coriolis force.
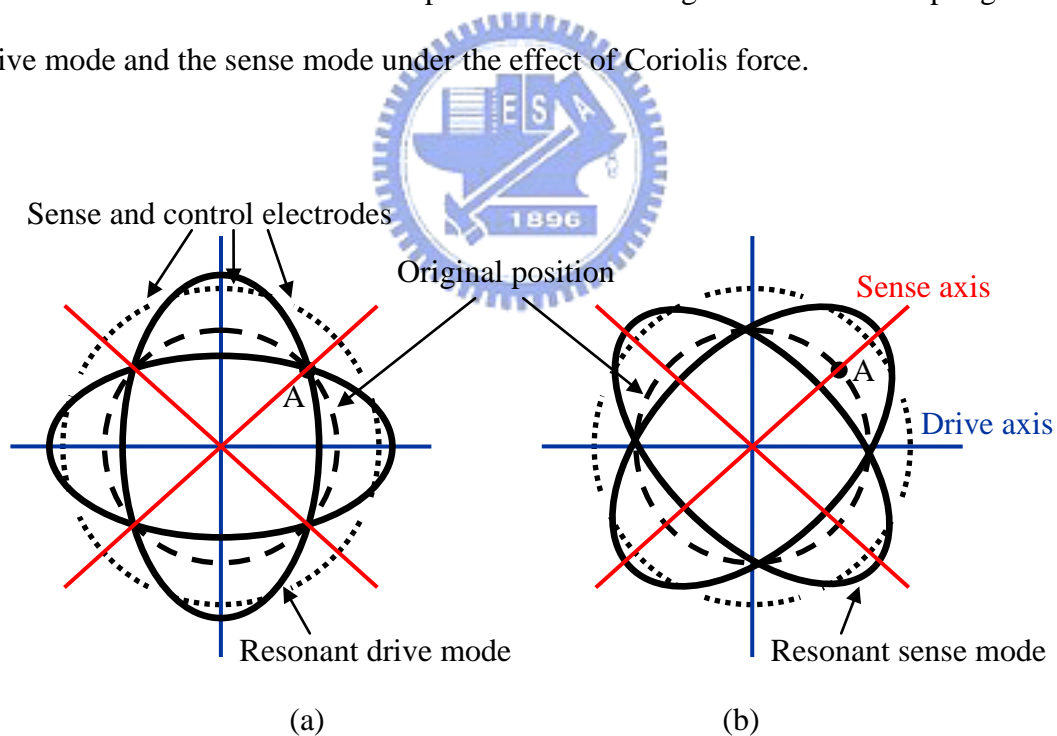
Fig. 2.3 Resonant modes of a vibrating ring gyroscope (a) drive mode, (b) sense mode

In Fig. 2.3, the vibration direction of the sense mode is the node direction of the drive mode. If the angular rate Ω≠0, the sense axis will be driven by the Coriolis

force. In this case, the displacement of node A is no longer zero; it is in direct proportion to Coriolis force.

2.1.1 Non-ideal effects

Usually there are non-ideal effects in the gyroscope, such as the system parameter variation, the quadrature errors, mismatch between the two resonant frequencies, etc.. The main reason of the system parameter variation is the fabrication process deviation. For instance, the etching rate of the structure decreases when the concentration of the etching solution decreases with time. The wear of the gyroscope would also change structure characteristics and cause system parameters to fall short of the requirements. The electrostatic spring softening effect is another important factor, too. The total spring constant of the structure decreases when the applied electrostatic force increases. If the amount of the static electricity is large enough, the parallel plate capacitor would even pull-in and the gyroscope would stop resonating until restarting the system.

The quadrature error is another major source of error in MEMS gyroscopes. It is related to the erroneous coupling of the drive motion into the sense motion in the absence of a rotational rate. This coupling is caused by imperfections in the manufacturing process. More particularly, the coupling will occur whenever the support structures of the vibrating element are not perfectly orthogonal. The output signal induced by such drive error is usually referred to as the quadratic signal. In general, it has been assumed that the damping around the ring is symmetric, which means the quadrature error term only appears in the stiffness part.

The other important non-ideal effect is the mismatch between the resonant frequencies. The vibrating ring gyroscope is a two-degree-of-freedom (2-DOF) dynamic system which includes drive and sense axes. The 2-DOF dynamic system

15

has two independent resonant frequencies, one is the drive mode resonant frequency $\omega_x = \sqrt{k_x/m}$, and the other is the sense mode resonant frequency $\omega_y = \sqrt{k_y/m}$. When the stiffness values in the drive and sense directions are the same, i.e. $k_x = k_y$ then the two resonance modes are matched, i.e. $\omega_x = \omega_y$. However, fabrication imperfections and environmental changes may drastically affect the suspension stiffness. If $\omega_x \neq \omega_y$, the frequency response of the 2-DOF system has two resonant peaks, one at ω_x, and one at ω_y. On the other hand, if $\omega_x = \omega_y$, the frequency response of the 2-DOF system has one combined resonant peak, which will provide a much larger response amplitude due to coinciding drive and sense resonance peaks, as shown in Fig. 2.4.
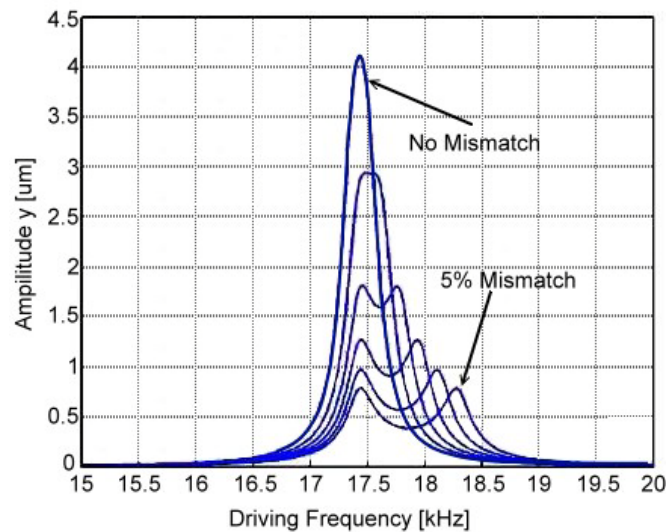
Fig. 2.4 Response of the overall 2-DOF system with varying drive and sense stiffness mismatch [6].

2.1.2 Open-loop mode of operation

In the operation of gyroscopes, the drive axis is driven to resonance and the Coriolis force along the sense axis is detected. Both open-loop and closed-loop modes of operation can be implemented.

Many MEMS gyroscopes are operated in open-loop mode due to its easy

16

implementation and direct control method. In an open-loop system, the driving force is only applied to the drive mode. Then the displacement of the sense axis caused by the Coriolis force is detected, which is in direct proportion to the angular rate Ω.

The disadvantage of this mode is longer rise and the settling times. It can not be used when there are the quadrature error and system variation either.

2.1.3 Closed-loop mode of operation

In the closed-loop operation of the gyroscope, a feedback force is applied to the sense mode to counteract the Coriolis force, thus maintaining the amplitude of the sense mode at zero. The feedback force is therefore an indication of the magnitude of the angular rate. The disturbance and noise can be eliminated in the closed-loop mode. In this thesis, the closed-loop method will be applied to design the controller.
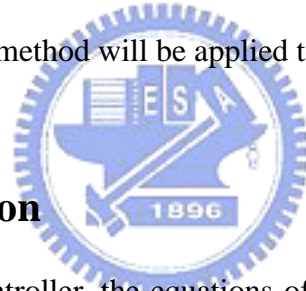
2.2 Equation of motion

Before designing the controller, the equations of motion and system parameters are derived.

2.2.1 Ideal plant

The MEMS gyroscope is modeled as a 2-DOF spring-mass-damper system with the drive mode displacement x and sense mode displacement y. The two modes are coupled by the Coriolis force. The governing equation of the ideal vibrating ring gyroscope can be expressed as:

$$\begin{bmatrix} m & 0 \\ 0 & m \end{bmatrix}\begin{bmatrix} \ddot{x} \\ \ddot{y} \end{bmatrix} + \begin{bmatrix} b & -2m\Omega \\ 2m\Omega & b \end{bmatrix}\begin{bmatrix} \dot{x} \\ \dot{y} \end{bmatrix} + \begin{bmatrix} k & 0 \\ 0 & k \end{bmatrix}\begin{bmatrix} x \\ y \end{bmatrix} = \begin{bmatrix} F_x \\ F_y \end{bmatrix} \tag{2.1}$$

where m is the equivalent mass at resonant frequency, b is the damping coefficient, Ω is the angular rate, k is the spring constant, F_x and F_y are applied forces on the drive

and sense axes, respectively. The governing equation can be normalized and rewritten as:

$$\begin{bmatrix} 1 & 0 \\ 0 & 1 \end{bmatrix}\begin{bmatrix} \ddot{x} \\ \ddot{y} \end{bmatrix} + \begin{bmatrix} 2\xi\omega & -2\Omega \\ 2\Omega & 2\xi\omega \end{bmatrix}\begin{bmatrix} \dot{x} \\ \dot{y} \end{bmatrix} + \begin{bmatrix} \omega^2 & 0 \\ 0 & \omega^2 \end{bmatrix}\begin{bmatrix} x \\ y \end{bmatrix} = \begin{bmatrix} u_x \\ u_y \end{bmatrix} \tag{2.2}$$

where ω is natural frequency of two axes, ξ is damping coefficient, u_x and u_y are control inputs for the drive and sense axes. The equation of motion, Eq. 2.1, can be rewritten as state equations.

$$\begin{bmatrix} \dot{x} \\ \ddot{x} \\ \dot{y} \\ \ddot{y} \end{bmatrix} = \begin{bmatrix} 0 & 1 & 0 & 0 \\ -\omega^2 & -2\xi\omega & 0 & 2\Omega \\ 0 & 0 & 0 & 1 \\ 0 & -2\Omega & -\omega^2 & -2\xi\omega \end{bmatrix}\begin{bmatrix} x \\ \dot{x} \\ y \\ \dot{y} \end{bmatrix} + \begin{bmatrix} 0 & 0 \\ \dfrac{1}{m} & 0 \\ 0 & 0 \\ 0 & \dfrac{1}{m} \end{bmatrix}\begin{bmatrix} F_x \\ F_y \end{bmatrix} \tag{2.3}$$

$$\begin{bmatrix} x \\ y \end{bmatrix} = \begin{bmatrix} 1 & 0 & 0 & 0 \\ 0 & 0 & 1 & 0 \end{bmatrix}\begin{bmatrix} x \\ \dot{x} \\ y \\ \dot{y} \end{bmatrix}$$

If the angular rate is zero, this equation can be decoupled into two transfer functions as:

$$\frac{X(s)}{F_x(s)} = \frac{Y(s)}{F_y(s)} = \frac{1}{k + bs + ms^2} \tag{2.4}$$

The system then becomes two single-input single-output (SISO) systems, which can be controlled by PID controllers.

2.2.2 Non-ideal plant

Because of the non-ideal effects described in section 2.1.1, the governing equation has to be corrected as

$$\begin{bmatrix} m & 0 \\ 0 & m \end{bmatrix}\begin{bmatrix} \ddot{x} \\ \ddot{y} \end{bmatrix} + \begin{bmatrix} b_x & -2m\Omega+b_{xy} \\ 2m\Omega+b_{xy} & b_y \end{bmatrix}\begin{bmatrix} \dot{x} \\ \dot{y} \end{bmatrix} + \begin{bmatrix} k_x & k_{xy} \\ k_{xy} & k_y \end{bmatrix}\begin{bmatrix} x \\ y \end{bmatrix} = \begin{bmatrix} F_x \\ F_y \end{bmatrix} \tag{2.5}$$

where b_x, b_y, k_x, k_y are the damping coefficient and spring constant of two axes, b_{xy} and k_{xy} are the quadrature errors. The governing equation can be normalized and rewritten as:
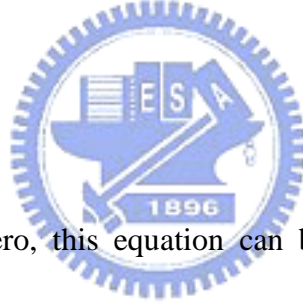
$$\begin{bmatrix} 1 & 0 \\ 0 & 1 \end{bmatrix} \begin{bmatrix} \ddot{x} \\ \ddot{y} \end{bmatrix} + \begin{bmatrix} 2\xi_x \omega_x & 0 \\ 0 & 2\xi_y \omega_y \end{bmatrix} \begin{bmatrix} \dot{x} \\ \dot{y} \end{bmatrix} + \begin{bmatrix} \omega_x^2 & 0 \\ 0 & \omega_y^2 \end{bmatrix} \begin{bmatrix} x \\ y \end{bmatrix} = \begin{bmatrix} u_x - \omega_{xy}^2 y + 2\Omega \dot{y} \\ u_y - \omega_{xy}^2 x - 2\Omega \dot{x} \end{bmatrix}$$

$$\begin{cases} \xi_x = \xi_0 + \Delta \xi_x \\ \omega_x = \omega_0 + \Delta \omega_x \end{cases}$$

$$\begin{cases} \xi_y = \xi_0 + \Delta \xi_y \\ \omega_y = \omega_0 + \Delta \omega_y \end{cases} \tag{2.6}$$

where ξ_0 is the nominal damping coefficient, ω_0 is the nominal natural frequency, $\Delta \xi_x$, $\Delta \xi_y$, $\Delta \omega_x$, $\Delta \omega_y$ are the variations of the respective parameters, and ω_{xy}^2 is the quadrature error caused by stiffness coupling. From Eq. 2.6, the transfer function of the drive and sense axes can be expressed as:

$$G_x(s) = \frac{X(s)}{U_x(s)} = \frac{1}{s^2 + 2\xi_x \omega_x s + \omega_x^2}$$

$$G_y(s) = \frac{Y(s)}{U_y(s)} = \frac{1}{s^2 + 2\xi_y \omega_y s + \omega_y^2} \tag{2.7}$$

where U_x and U_y are the control input of the drive and sense axes, respectively.

2.3 Parameters of the MEMS gyroscope

The layout of the micro vibrating ring gyroscope is shown in Fig. 2.5. The normalized equations of motion, as shown in Eq. 2.6, were applied to the controller design and simulation in this thesis.
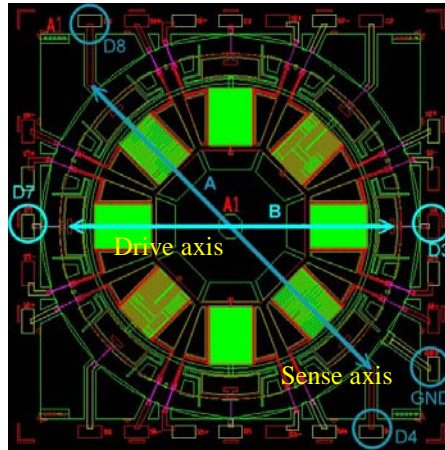
Fig. 2.5 layout of the micro vibrating ring gyroscope

Because the system is operated in the resonance mode, the modal analysis of the ring structure was first performed by using finite element method. The first four modes are shown in Fig. 2.6. Fig. 2.6(a) and Fig. 2.6 (b) are translation modes which are not the operation mode. Fig. 2.6 (c) and Fig. 2.6 (d) are the desired drive and sense modes. Because the frequencies of the two modes are assumed to match each other, the gyroscope is assumed to be operated in mode 3 whose resonance frequency is 10220Hz and equivalent mass is 1.251×10^{-6}kg.

In addition to the resonant frequency and the equivalent mass, the quality factor and damping coefficient are found experimentally. From the test data provided by Chung-Shan Institute of Science and Technology, the quality factor is about 450 and thus the damping coefficient is $\xi = 1/2Q = 1/900$. The structure thickness is 100μm, and the capacitance gap is 4.5μm.

(a) f_0=10071Hz (b) f_0=10100Hz

(c) f_0=10220Hz (d) f_0=10344Hz
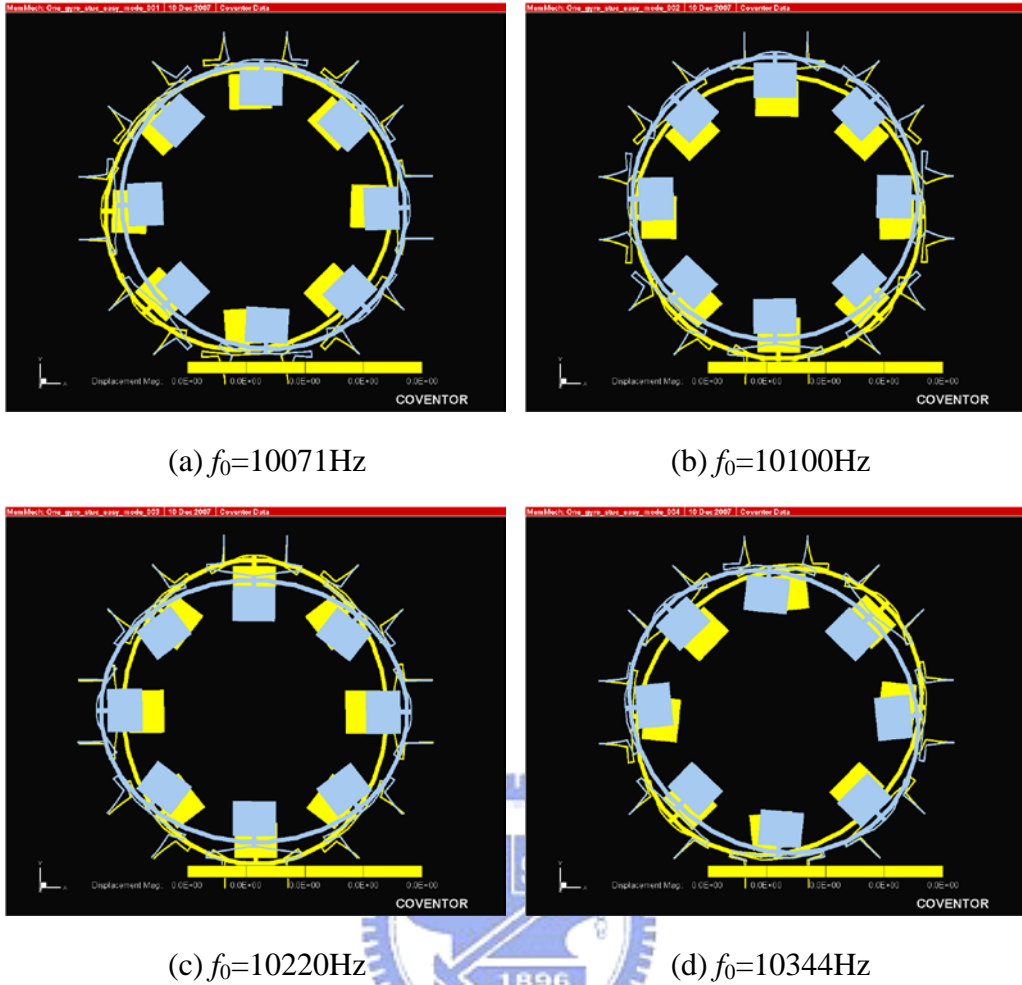
Fig. 2.6 Modal analysis (a) mode1, (b) mode2, (c) mode3, (d) mode4

The lumped and operation parameters of the system are shown in Table 2.1. Simulink was used to simulate the dynamic response of the system and the performance of the controller. System specifications are shown in Table 2.2. The amplitude of the drive axis is controlled at 1um, and the sense axis is assumed to be static. The maximum angular rate to be measured is 100°/sec. The allowed variation of the system parameters to be considered in this thesis is 10%. The settling time is 0.2ms and the maximum overshoot is 10%.

Table 2.1 System parameters

Structure thickness	100μm
Capacitance gap	4.5μm
Quality factor Q	450
Resonant frequency $f\,(\omega)$	10220Hz (64214rad/sec)
Equivalent mass	1.251×10^{-6}kg
Damping coefficient ξ	1.11×10^{-3}

Table 2.2 System specifications

Angular rate Ω	0~100°/sec (0~1.745rad/sec)
amplitude of drive axis	1μm
Maximum overshoot M_o	10%
Settling time t_s	0.2ms
Quadrature error ω_{xy}^2	6421.4rad/sec (10% of resonant frequency)
Uncertainty Δξ, Δω	10%

2.4 Force balance control

The concept of the force balance is often applied to the control of inertial sensors. Coriolis force is considered as a disturbance in the governing equation. The controller is designed to provide a feedback force to counteract the Coriolis force and the quadrature error to maintain the displacement of the sense axis at zero. Therefore, the coupled system can be modeled as two systems with the coupling viewed as disturbance, as shown in Fig. 2.7. The reference inputs of the two axes are $10^{-6}\sin\omega t$ and zero, respectively. The controller will be designed according to the loops in Fig. 2.7.

⟨ Drive axis ⟩

$$-\omega_{xy}^2 y + 2\Omega\dot{y}$$

⟨ Sense axis ⟩

$$-\omega_{xy}^2 x + 2\Omega\dot{x}$$
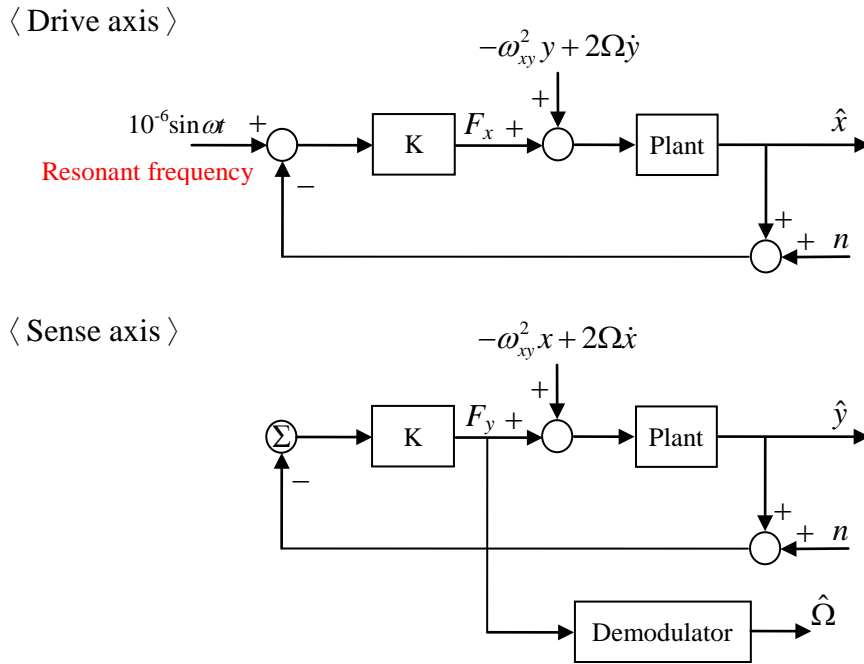
Fig. 2.7 Control loop of two axes

2.5 Demodulation

The rotation rate can be obtained through demodulation. In this thesis, the displacement of the sense axis is maintained at zero by a feedback force to cancel the Coriolis force and quadrature error terms from the drive axis. The normalized force can be expressed as:

$$u_y = \frac{F_y}{m} = -\omega_{xy}^2 x - 2\Omega\dot{x} \tag{2.8}$$

The angular rate Ω and the quadrature error ω_{xy}^2 can be derived by demodulating the feedback force u_y. If the displacement x of the drive axis is represented by a sinusoidal signal $x = A\sin\omega t$, the angular rate Ω can be demodulated from the feedback force u_y by the multiplication by $\cos\omega t$:

23

$$u_y \cdot \cos \omega t = \left(-\omega_{xy}^2 x - 2\Omega \dot{x} \right) \cdot \cos \omega t$$
$$= -\omega_{xy}^2 A \sin \omega t \cos \omega t - 2\Omega A \omega \cos^2 \omega t \qquad (2.9)$$
$$= -\frac{1}{2} \omega_{xy}^2 A \sin 2\omega t - \Omega A \omega \cos 2\omega t - \Omega A \omega$$

In Eq. 2.9, the high frequency signals $-\frac{1}{2}\omega_{xy}^2 A \sin 2\omega t$ and $-\Omega A \omega \cos 2\omega t$ can be filtered out by a low pass filter (LPF). Therefore, the angular rate Ω can be found from:

$$\Omega = F_{LPF}\left(-\frac{u_y \cdot \cos \omega t}{A\omega} \right), \qquad (2.10)$$

where $F_{LPF}(\cdot)$ represents the function of a low pass filter. In the same way, the quadrature error ω_{xy}^2 can be demodulated from the feedback force u_y by the multiplication of $\sin \omega t$:

$$\omega_{xy}^2 = F_{LPF}\left(-\frac{2u_y \cdot \sin \omega t}{A} \right) \qquad (2.11)$$

A second order filter attenuates higher frequencies more steeply than a first order filter. The transfer function of the filter is

$$F_{LPF}(s) = \frac{1}{(\tau s + 1)^2} \qquad (2.12)$$

where τ is a time constant. The rolloff is 40 dB per decade at high frequency. Because the resonant frequency is about 10000Hz, the time constant τ of the low pass filter is chosen as 1×10^{-4}, so that the high frequency (2ω) signals are attenuated by 12 dB.

2.6 Summary

In this chapter, the operating principle of the micro vibrating ring gyroscope, source and effects of system variation, and system parameters are presented.

Closed-loop control is used in this research. The displacement of the drive axis is to be controlled at the constant amplitude of 1μm; the displacement of the sense axis is to be maintained at zero. A feedback force is used to counteract the disturbance caused by Coriolis force and quadrature error. The angular rate Ω can be derived by demodulating the feedback force. The controller design will be discussed in Chapter 3.

Chapter 3   Controller design

The objectives of this research are to eliminate disturbance and to deal with parameter uncertainty. PID control is a general industrial control method and the QFT/H$_\infty$ control is a robust control method. These two methods are used to design the controllers in this chapter. The performances of these two controllers are compared by Simulink system in Chapter 4.

3.1 System analysis

In Chapter 2, the governing equations of the MEMS gyroscope and the system parameters were presented. From Eq. 2.4 and Table 2.1, the uncoupled transfer functions of the two axes are as follows:

$$G(s) = \frac{1/m}{s^2 + 2\zeta\omega s + \omega^2} = \frac{7.99 \times 10^5}{s^2 + 142.7s + 4.123 \times 10^9} \tag{3.1}$$

In this section, the characteristics of the transfer function in time domain and frequency domain are discussed.

3.1.1 Characteristics in time domain

If the Coriolis force is considered as an internal disturbance of the system, the government equation of the gyroscope can be decoupled to two independent transfer functions for the two axes, as shown in Eq. 3.1. For this standard second order system with the natural frequency $\omega = 64214 \text{ rad}/\sec$ and damping coefficient $\xi = 1/900$, the maximum overshoot M_o and settling time t_s of the step response are [19]:

$$M_o = e^{-\pi\xi/\sqrt{1-\xi^2}} = 99.65\%$$
$$t_s = \frac{4.6}{\xi\omega} = 0.064\sec \tag{3.2}$$

The MATLAB simulation of the step response of the plant is shown in Fig. 3.1. From Eq. 3.2 and Fig. 3.1, the maximum overshoot is too large and the settling time of the open-loop system is too long. Therefore, a controller is needed to improve the transient response performance. The characteristic in frequency domain is listed in Table 3.1.
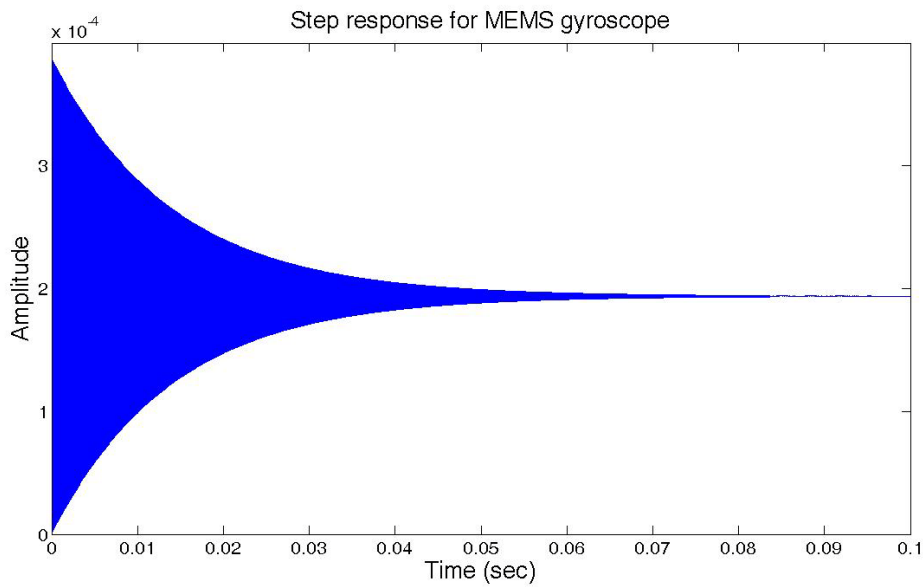
Fig. 3.1 Step response of MEMS gyroscope

3.1.2 Characteristics in frequency domain

In frequency domain, the dominant poles of the uncoupled transfer function Eq. 3.1 are derived as $-71.35 \pm 64214 j$. The Bode plot is shown in Fig. 3.2. The original gain margin is infinite, and the phase margin is only $0.18°$. If the gyroscope is operated in resonant frequency, it will have the largest amplitude and the drive voltage can be reduced. The characteristic in frequency domain is also listed in Table 3.1.
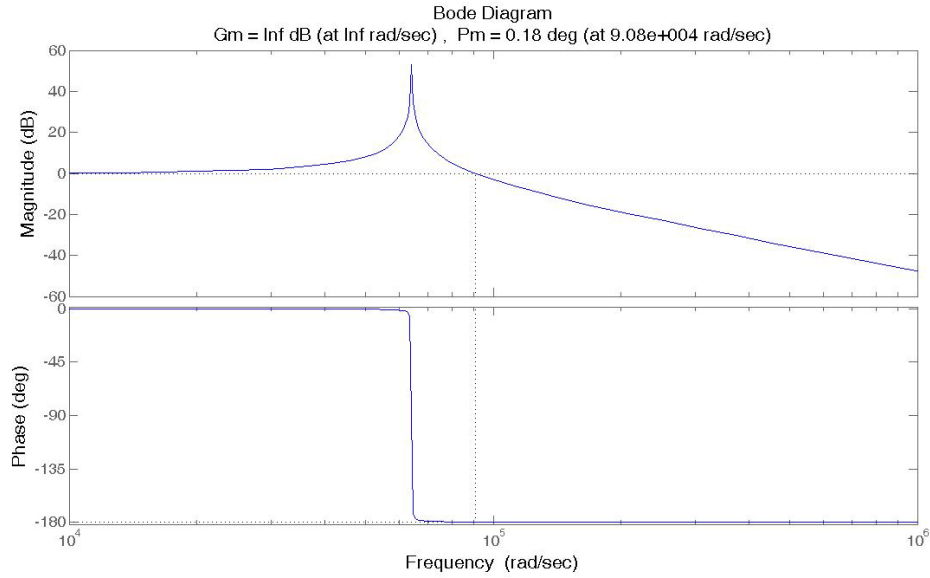
Fig. 3.2 Bode plot of MEMS gyroscope plant

Table 3.1 Characteristics in time and frequency domains

Time Domain	
Maximum overshoot M_o	99.65%
Settling time t_s (within 1%)	0.064sec
Rise time t_r (from 10% ~ 90%)	0.024ms
Frequency Domain	
Dominant pole	$-71.35 \pm 64214\,j$
Gain margin	∞
Phase margin	$0.18°$

3.2 PID control design using pole placement

A proportional–integral–derivative (PID) controller is a generic control loop feedback mechanism widely used in industrial control systems. A PID controller attempts to correct the error between a measured variable and a desired set-point by calculating and then outputting a corrective action. The controller can be design by moving the poles to the new locations to satisfy the specifications.

3.2.1 PID controller

Once the transfer function of the system is derived, the corresponding PID controller can be designed. The schematic of the closed-loop system with the PID controller is shown in Fig. 3.3.
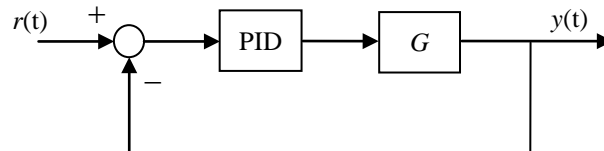
Fig. 3.3 Schematic of the closed-loop system with a PID controller

The PID controller includes three parameters: the Proportional, the Integral and the Derivative gains. The Proportional gain determines the reaction to current error, the Integral gain determines the reaction based on the sum of plant errors and the Derivative gain determines the reaction to the rate at which the error has been changing. The transfer function of a PID controller is

$$G_c(s) = K_p \left(1 + \frac{1}{T_i s} + T_d s \right) = K_p + \frac{K_i}{s} + K_d s \tag{3.3}$$

where K_p is the proportional gain, $K_i = K_p / T_i$ is the integral gain, and $K_d = K_p T_d$ is the derivative gain. Because the specifications have been defined, the PID controller can be designed by pole placement [20] to move the poles to the appropriate place to satisfy the specifications.

3.2.2 Pole placement method

Pole placement is one of the control methods to make the system satisfy the specifications by moving the poles of the system to the appropriate places. In a closed-loop system, the pole placement has a direct effect on time response, such as

rise time, settling time, maximum overshoot, etc.. The design starts with an assumption of what form the controller must take in order to control the given plant. Typically, specifications lead to the formation of a second order equation. Most of the final characteristic equation will have more than 2 poles, and additional desired poles must be determined. Algebra is used to determine the controller coefficients necessary to achieve the desired closed-loop poles with the assumed controller form. Typically, an integrator is used to drive the steady-state error towards zero. This implies that the final characteristic equation will have at least one more pole than uncontrolled system.

3.2.3 Using pole placement to design PID controller

From Eqs. 3.1 and 3.3, the characteristic equation of the closed-loop system with a PID controller, $1+G_cG = 0$, can be expressed as:

$$
\begin{aligned}
\Phi_{CL} &= \left(s^2 + 2\xi\omega s + \omega^2\right)s + \frac{1}{m}\left(K_d s^2 + K_p s + K_i\right) \\
&= s^3 + \left(2\xi\omega_n + \frac{1}{m}K_d\right)s^2 + \left(\omega^2 + \frac{1}{m}K_p\right)s + \frac{1}{m}K_i
\end{aligned}
\tag{3.4}
$$

The desired characteristic equation is determined by the maximum overshoot and settling time in the specifications. Because there are three poles in Eq 3.4, it can be expressed as $(s+a)\left(s^2 + 2\xi_{\text{desired}}\omega_{\text{desired}}s + \omega^2_{\text{desired}}\right)$, where a is an extra pole. Comparing the coefficients of the desired characteristic equation with the closed-loop characteristic equation Eq. 3.4, the PID gains can be solved.

In the time domain specifications, the maximum overshoot is 10% and the settling time is 0.2ms. So the desired damping coefficient ξ_{desired} is 0.591 and the desired natural frequency ω_{desired} is 38300rad/sec from Eq.3.2. The extra pole is supposed to be at ten times of the natural frequency. But it was found in simulation that such an extra pole would make the closed-loop system unstable. Therefore, the

extra pole was placed at 1000x of the natural frequency, $a = -3.83 \times 10^7$. The desired characteristic equation of the closed-loop can be expressed as:

$$\Phi_{CL} = \left[s^2 + 45194s + \left(3.83 \times 10^4\right)^2 \right]\left(s + 3.83 \times 10^7\right) \tag{3.5}$$

The three gain parameters of the PID controller can be obtained by comparing Eq. 3.5 with Eq. 3.4, as listed in Table 3.2.

Table 3.2 PID controller gain

	Result
K_p	418.6
K_i	1.363×10^7
K_d	9.3×10^{-3}
PID	$G_c(s) = \dfrac{9.3 \times 10^{-3} s^2 + 418.6s + 1.363 \times 10^7}{s}$

3.3 QFT/H$_\infty$ Control

Both Quantitative Feedback Theory (QFT) and H$_\infty$ design techniques have be developed for a long time [21]. The QFT and H$_\infty$ design techniques are popular robust feedback control schemes which can achieve the desired system objectives no matter if there is any uncertainty. In this thesis, the two methods will be applied to design the controller. The standard schematic of the closed-loop system by QFT/H$_\infty$ design method is shown in Fig. 3.4.
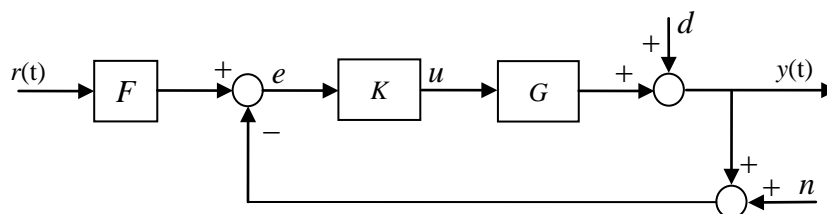

Fig. 3.4 Schematic of the general closed-loop system with QFT/H$_\infty$ controller

3.3.1 QFT design technique

QFT was first introduced by Horowitz and Sidi [21]. This method translates the time domain specification to the frequency domain and uses Nichols Chart to find the boundary conditions. It also makes the system output satisfy the desired specifications by moving the poles and the zeros of the controller to the suitable positions.

The general problem is how to design the controller K and prefilter F in Fig. 3.4. Fig. 3.4 is a two degrees of freedom (TDOF) feedback system, which includes plant P, controller K, prefilter F, input signal r, output signal y, disturbance d, and sensor noise n. The controller K is the first design degree of freedom used to reduce system sensitivity from disturbance and noise. The prefilter F is the second design degree-of-freedom used to satisfy the required performance. Thus the plant output is bounded and constrained by the given specifications.

Two boundary conditions in time domain, B_u and B_l, are given, so that the output $y(t)$ is bounded by:

$$B_l(t) \le y(t) \le B_u(t) \tag{3.6}$$

These tracking specifications in the time domain are translated into the frequency domain as the upper bound and the lower bound, as shown in Fig. 3.5,

$$B_l(\omega) \le \left| T(j\omega) \right| \le B_u(\omega) \tag{3.7}$$

where

$$\frac{Y(s)}{R(s)} = T(s) = F(s)T_1(s)$$

$F(s)$ is a prefilter, and $\qquad\qquad\qquad\qquad\qquad\qquad\qquad$ (3.8)

$T_1(s) = \dfrac{K(s)G(s)}{1 + K(s)G(s)}$ is the loop gain.

Because the QFT theory is part of the robust control design, the sensitivity is the most important factor in studying the parameter variation effect. The definition of

sensitivity specification is expressed as [17]:

$$S_G^T(s) \equiv \frac{\partial T/T}{\partial G/G} \cong \frac{\Delta T/T}{\Delta G/G} \quad \text{or} \quad \left| S_G^T(s) \right| \equiv \frac{\Delta \left| T(j\omega) \right|_{\max}}{\Delta \left| G(j\omega) \right|_{\max}} \tag{3.9}$$

where $\Delta \left| T(j\omega) \right|_{\max}$ and $\Delta \left| G(j\omega) \right|_{\max}$ are the maximum variation of $\left| T(j\omega) \right|$ and $\left| G(j\omega) \right|$, which is 10% in this thesis. In the QFT theory, the upper bound is an under damped system, $\xi < 1$, and the lower bound is an over damped system, $\xi > 1$. Thus, the specifications in time domain can be applied to set the upper bound and the lower bound conditions.

With the given boundary condition, Nichols Chart is applied to design the controller. In this thesis, the controller is designed by H$_\infty$ method. The prefilter F(s) will move the closed loop gain T_1(s) to within the upper bound and the lower bound, as shows in Fig. 3.5, to fit the specifications by adding poles and zeros.
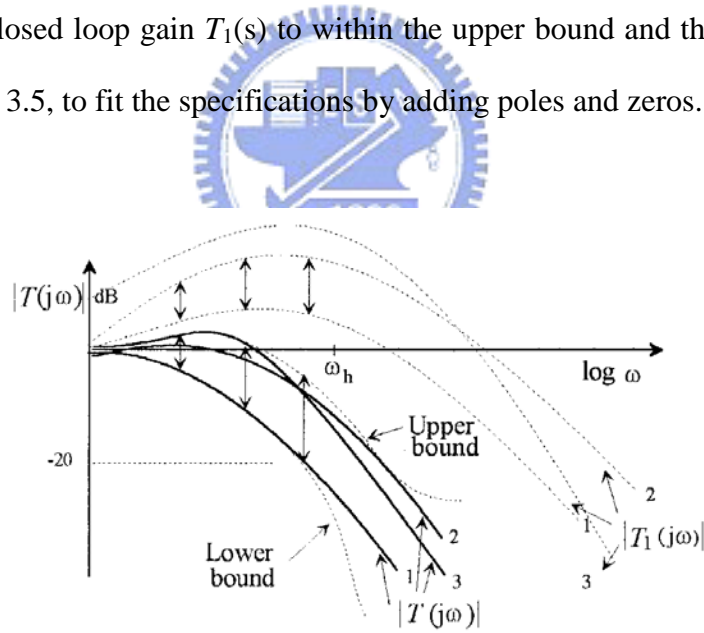

Fig. 3.5 Unity feedback closed-loop for different plant cases [17]

3.3.2 H$_\infty$ control method [22]

The H$_\infty$ control method is applied to design a robust controller when system parameters change or disturbance exists. In the H$_\infty$ control theory, as shown in Fig. 3.6, K is the controller and G is the generalized plant including the plant and the weighting

functions. It can be written as:

$$\begin{bmatrix} z \\ y \end{bmatrix} = G \begin{bmatrix} w \\ u \end{bmatrix} = \begin{bmatrix} G_{11} & G_{12} \\ G_{21} & G_{22} \end{bmatrix} \begin{bmatrix} w \\ u \end{bmatrix} \tag{3.10}$$

where w is a vector signal including noises, disturbances, and reference signals, z is a vector signal including all controlled signals and tracking errors, u is the control signal, y is the measurement.
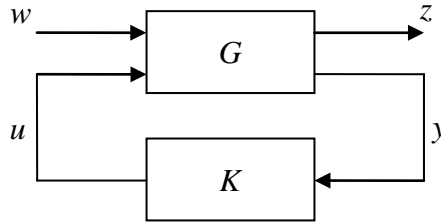
Fig. 3.6 H$_\infty$ control structure

According to Eq. 3.10, the transfer functions of w and z are derived as shown below:

$$z = \left[G_{11} + G_{12}K\left(I - G_{22}K\right)^{-1} G_{21} \right] w \equiv T_{zw}w$$

$$T_{zw} = G_{11} + G_{12}K\left(I - G_{22}K\right)^{-1} G_{21} \tag{3.11}$$

where T_{zw} is transfer matrix of w to z. The purpose of H$_\infty$ control is to design a controller K to suppress the controlled value z. The magnitude of T_{zw} is defined by the H$_\infty$ norm and can be expressed as:

$$\left\| T_{zw} \right\|_\infty = \sup_\omega \bar{\sigma}\left\{ T_{zw}\left(j\omega \right) \right\} \tag{3.12}$$

where $\bar{\sigma}(\cdot)$ means the maximum singular value, and $\sup(\cdot)$ means supremum or least upper bound, and is defined as the smallest real number that is greater than or equal to this number. It is the maximum value of the gain in the Bode plot, and the maximum distance to the origin in the vector diagram. According to the input signal and the output signal shown in Fig. 3.6, the H$_\infty$ norm of T_{zw} can be redefined as

$$\left\| T_{zw}(s) \right\|_{\infty} = \sup_{\omega} \frac{\left\| z \right\|_2}{\left\| w \right\|_2} \tag{3.13}$$

From Eq. 3.13, it can be observed that the problem of H$_\infty$ control is to minimize the transfer matrix of w to z in the form of H$_\infty$ norm, and satisfy $\left\| T_{zw}(s) \right\|_{\infty} < \gamma$, which γ is the chosen positive number.

3.3.3 Combined QFT/H$_\infty$ control

The combined QFT/H$_\infty$ control method does not use the Nichols Chart to design the controller. Instead, the controller K is first calculated by the H$_\infty$ optimization control method, and then the prifilter F is added to make the output fit the performance requirement. The design steps are shown in Fig. 3.7, where the most important part of the design is to transfer the specifications of the system into appropriate weighting functions. Step 1 is finding out the weighting function, and translating into the H$_\infty$ control structure as shown in Fig. 3.6. Step 2 is using H$_\infty$ method to calculate controller K, and using the boundary condition to define prefilter F.

The closed-loop system with the controller K can be stabilized by minimizing the sensitivity and the disturbance w can have the minimal effect on the expectable output z. A function $D(\omega)$ is given to specify the disturbance rejection specifications, and the sensitivity function has satisfied $\left| S(j\omega) \right| \le D(\omega)$. The sensitivity function is constrained to satisfy this inequality $\left| W_1(j\omega) S(j\omega) \right| \le 1$, where the weighting function W_1 is used to limit the sensitivity function and can be chosen by

$$\left| W_1(j\omega) \right| \le \frac{D(\omega)}{\left| S(j\omega) \right|}.$$

〈 Step 1 〉

〈 Step 2 〉
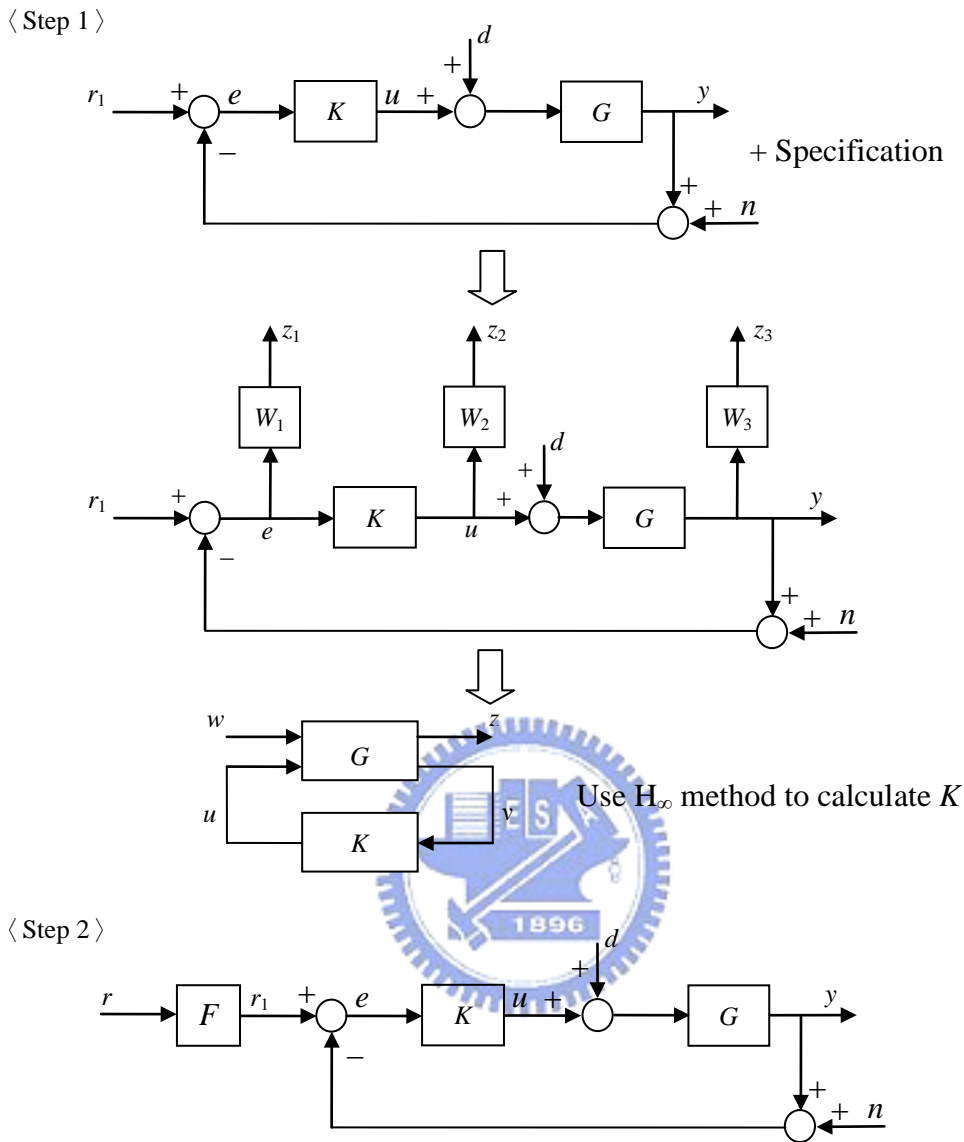
Fig. 3.7 QFT/H$_\infty$ design step

The sensor noise amplification is not expected to exist in high frequency. If the high sensor noise amplification can be reduced, the cost of feedback design can be also reduced. After given nominal plant G_0, the transfer function from noise n to controller output u is $T_{un} = \dfrac{u}{n} = \dfrac{-K}{1+KG_0}$. It stands for the amplifier effect of the sensor noise. The weighting function W_2 has to satisfy $\left|W_2(j\omega)T_{un}(j\omega)\right| \leq 1$. A good control system should have proper loop-gain, which reduces the sensor noise at high

frequency. This property is considered in choosing W_2 and W_1. It is found practical and efficient here to use the control weighting function W_2 as a tuning parameter in optimization process.

Considering the parameter variations, if the multiplicative perturbation modeling structure of the plant is used [17], as shown in Fig. 3.8, then G can be represented by $G = G_0 (I + \Delta G)$, where ΔG is the error of multiplicative model. This structure allows the modeling of various plant uncertainties, and the condition for stable closed-loop systems [22, 23] is

$$\left\| \frac{KG_0}{1 + KG_0} \right\|_\infty < \frac{1}{\|\Delta G\|_\infty} \quad \text{or} \quad \left\| \Delta P \cdot \frac{KG_0}{1 + KG_0} \right\|_\infty \equiv \|W_3 \cdot T\|_\infty < 1 \qquad (3.14)$$

Therefore, the weighting function W_3 can be found by $\left\| \frac{G(j\omega)}{G_0(j\omega)} - 1 \right\|_\infty < |W_3(j\omega)|$. It is used to limit the complementary sensitivity function $T=1-S$ and to ensure the closed-loop system of multiplicative perturbation model is stable.
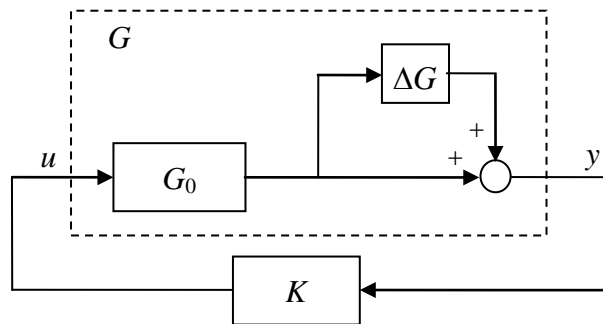

Fig. 3.8 Multiplicative perturbation model of the plant

In short, the three weighting functions satisfying Eq. 3.15 are necessary and sufficient for the solution of the proposed QFT/H$_\infty$ design technique.

$$\|W_1(j\omega)S(j\omega)\|_\infty \le 1$$
$$\|W_2(j\omega)T_{un}(j\omega)\|_\infty \le 1 \tag{3.15}$$
$$\|W_3(j\omega)T(j\omega)\|_\infty \le 1$$

3.3.4 Design of QFT/H$_\infty$ controller for MEMS gyroscope

The flow chart of the QFT/H$_\infty$ design method is shown in Fig. 3.9. First, the settling time and maximum overshoot specifications are applied to define the upper bound and lower bound. The upper bound uses the specifications to calculate that the damping coefficient $\xi = 0.59$ and natural frequency $\omega_n = 38301$. Since the lower bound is an over damped system, the damping coefficient is assumed as $\xi = 1.1$, and the natural frequency is shown as $\omega_n = 20543$. The two bounds are defined as $B(s) = \omega_n^2 / (s^2 + 2\xi\omega s + \omega_n^2)$ and can be expressed as:

$$B_u(s) = \frac{1.467 \times 10^9}{s^2 + 45194s + 1.467 \times 10^9}$$
$$B_l(s) = \frac{4.22 \times 10^8}{s^2 + 45194s + 4.22 \times 10^8} \tag{3.16}$$

To relax the restrictions in high frequency and to maintain the system performances, the pole (s+3.83×10^5) to the lower bound and the zero (s+2.05×10^5) to the upper bound are added. The two bounds become

$$B_u(s) = \frac{1.467 \times 10^9 \left(1 + \dfrac{s}{3.83 \times 10^5}\right)}{s^2 + 46194s + 1.467 \times 10^9}$$
$$B_l(s) = \frac{4.22 \times 10^8}{\left(s^2 + 46194s + 4.22 \times 10^8\right)\left(1 + \dfrac{s}{2.05 \times 10^5}\right)} \tag{3.17}$$

The three weighting functions of the plant are found by Eq. 3.15 and Fig. 3.9,

$$W_1(s) = \frac{s^2 + 1.018 \times 10^8 s + 3.142 \times 10^{13}}{70128s^2 + 140.26s + 0.0701}$$
$$W_2(s) = 0.1 \tag{3.18}$$
$$W_2(s) = 39$$

After the weighting functions are found, the "hinflmi" instruction in MATLAB is used to solve for the LMI-based H_∞ controller. The prefilter F is then added to adjust the frequency response so that it completely lies between the upper bound and the lower bound. The controller and the prefilter are as follows:

$$K(s) = \frac{1.885 \times 10^{10}(s+28.34)(s^2+2.324 \times 10^4 s + 4.121 \times 10^9)}{(s+0.02)(s+0.0014)(s^2+6.875 \times 10^5 s + 1.193 \times 10^{11})}$$

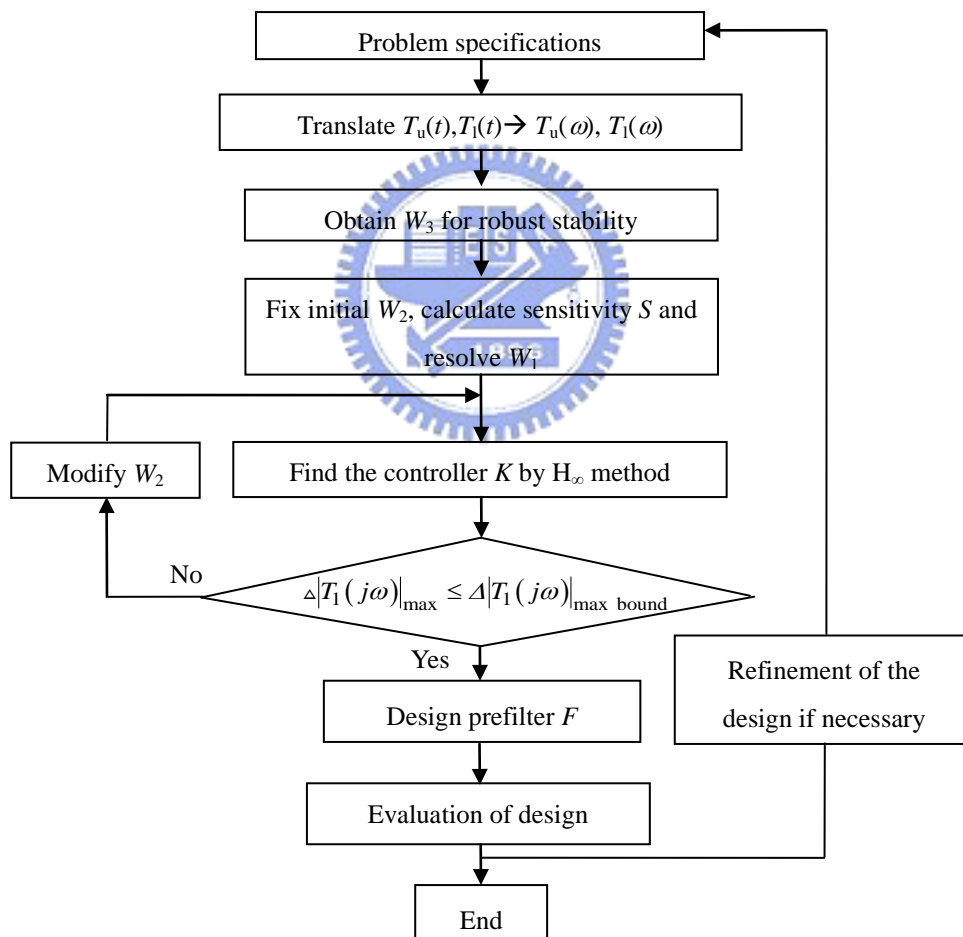$$F(s) = \frac{0.132\ (s+2.5 \times 10^5)\ (s+2 \times 10^5)}{(s+6 \times 10^4)\ (s+5 \times 10^4)}$$

(3.19)

Fig. 3.9 Flow chart of combined QFT/H_∞ design

The frequency response of the system with controller and prefilter is shown in Fig. 3.10. The red solid lines are the response of the family of plants with 10% variation in natural frequency and damping coefficient, as described in section 2.3.
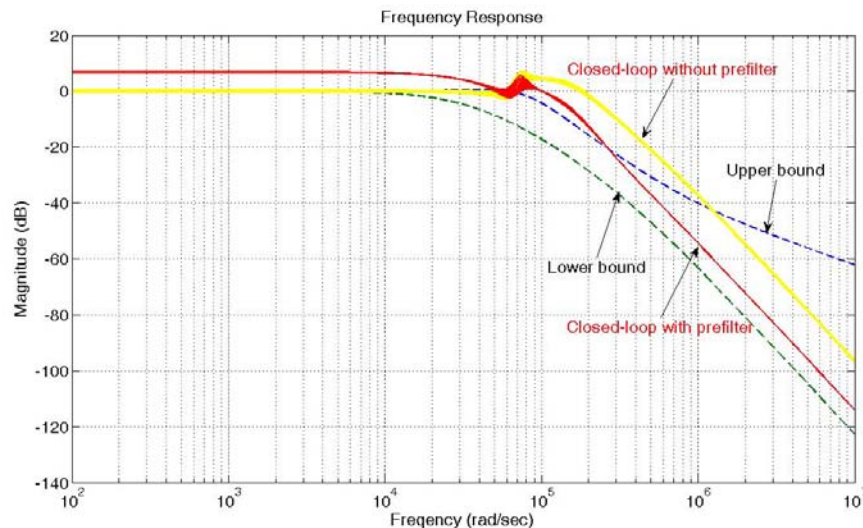

Fig. 3.10 Frequency response of the closed-loop system, $x(s)/r(s)$, with controller designed by QFT/H$_\infty$ method

3.3.5 QFT/H$_\infty$ method discussion

The QFT/H$_\infty$ control method discussed above is different from conventional QFT/H$_\infty$ control in a number of aspect. In this thesis, the Coriolis force and the quadrature error are regarded as inner disturbances of the system before the plant, as shown in Fig. 3.7. But in standard QFT/H$_\infty$ control method, the disturbances are after the plant, as shown in Fig. 3.4. Therefore, the way of deriving the weighting functions needs to be modified.

3.4 Summary

A PID controller and a QFT/H$_\infty$ controller are designed according the same

specifications. The former is the general control method and can be easily realized. The latter is a robust controller over fabrication errors and model uncertainties. The simulation results with the two controllers and the robustness comparison are presented in Chapter 4.

Chapter 4 Simulation and Discussion

This Chapter presents the Simulink simulation of the open-loop system, the PID control, QFT/H$_\infty$ control, and comparison with other publications. The reference position of the drive mode has an amplitude of 1µm at the resonance of 64214 rad/sec. The angular rate 100°/sec is added to the system at $t = 0.1$sec. The Simulink model of the plant is shown in Fig. 4.1. All the simulation is with double precision of 10^{-14}.
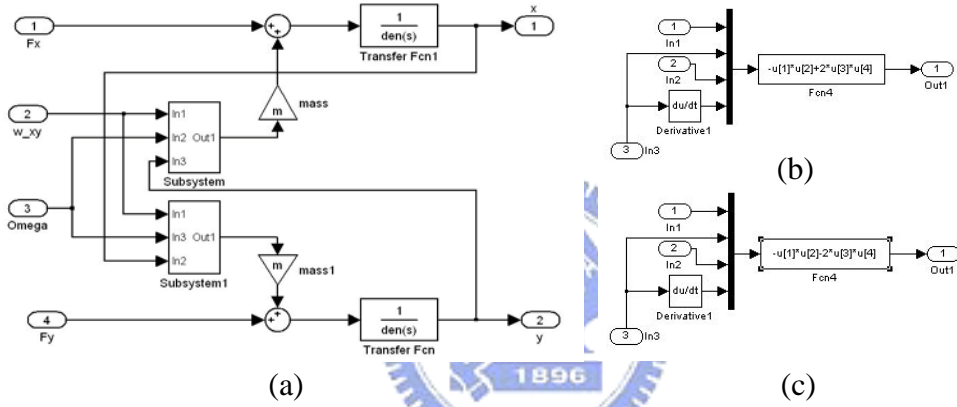

Fig. 4.1 Simulink model of the gyroscope (a) overview (b) detail of Subsystem for drive axis (c) detail of Subsystem for sense axis

4.1 Open-loop system

The governing equation of the drive axis can be rewritten as:

$$F_x = m\ddot{x} + b\dot{x} + kx = m\left(\ddot{x} + 2\xi\omega\dot{x} + \omega^2 x\right) \tag{4.1}$$

The desired trajectory of the drive axis is $x = A\sin\omega t$, $\dot{x} = A\omega\cos\omega t$ and $\ddot{x} = -A\omega^2\sin\omega t$, where $A = 1\times10^{-6}$m. The other parameters can be found in Table 2.1. In the ideal case, the drive force to drive the displacement of the drive axis at 1µm at the resonant frequency can be found from Eq. 4.1 as $F_x = 1.15\times10^{-5}\cos 64214t$ N. The Coriolis force from sense axis is ignored in the calculation because the displacement

of the drive axis is much larger than the displacement of the sense axis. Because the displacement of the sense axis is to be maintained at zero, the reference input of the sense axis is zero. For an open-loop system, only the Coriolis force acts on the sense axis. The governing equation of the sense axis can be expressed as:

$$F_y = -2m\Omega\dot{x} = m\ddot{y} + b\dot{y} + ky = m\left(\ddot{y} + 2\xi\omega\dot{y} + \omega^2 y\right) \tag{4.2}$$

With $\Omega = 100°/\text{sec}$ and other parameters from Table 2.1, Eq. 4.2, becomes:

$$1.251\times10^{-6}\left(\ddot{y} + 142.7\dot{y} + 4.123\times10^{9}y\right) = -2.8\times10^{-7}\cos(64214t) \tag{4.3}$$

The differential equation can be solved and the displacement of the sense axis is found as $y = -2.44\times10^{-8}\sin(64214t)\,\text{m}$.

4.1.1 Model verification

The force derived from Eq. 4.1, $F_x = 1.15\times10^{-5}\cos 64214t$ N, can be used to drive the lumped model Eq. 2.1, which has a quality factor Q = 450, to a displacement of 1μm at resonance. However, the same force, when applied to finite element modeling, will cause a displacement larger than that allowed by the spring structures outside the vibrating ring due to a much larger quality factor in the numerical calculation. Therefore, the force is reduced by a factor of 100 to $F_x' = 1.15\times10^{-7}\cos 64214t$ N before it is used in the finite element modeling to verify the lumped model. As shown in Fig. 4.2, a pair of sinusoidal forces F_x' in opposite directions are exerted on the ring in the direction of the drive axis. The deformation of the structure at resonance is shown in Fig. 4.3. As shown in Fig. 4.4, the maximum displacement of $x = 4.32\mu\text{m}$ occurs at $f = 10220.37\text{Hz}$, which is the same as that used in the lumped model. The displacement at low frequency is $4.3\times10^{-5}\mu\text{m}$. The quality factor of the system in the simulation can be derived as 1×10^{5}.

The reduced force F_x' drives the finite element model to a displacement of 4.32μm at resonance, but only to a displacement of 0.01μm in the lumped model. This means the quality factor of the finite element model is 432 times larger than that of the lumped model. However, the ratio of the two factors is only $Q_{finite\ element}/Q_{lumped} = 1×10^5/450 = 222$. The difference may be due to the numerical errors and should be discussed in the future.
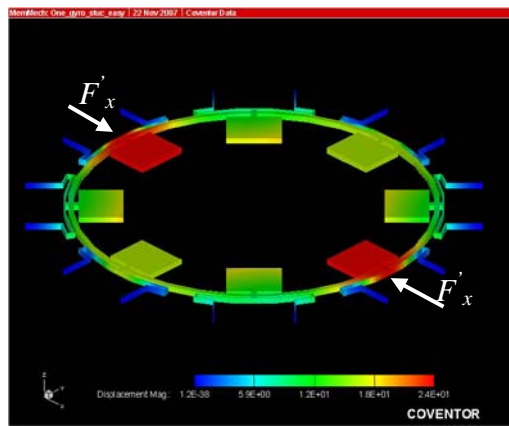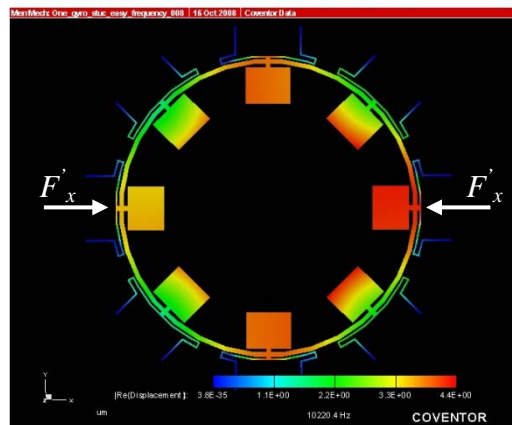

Fig. 4.2 Harmonic analysis

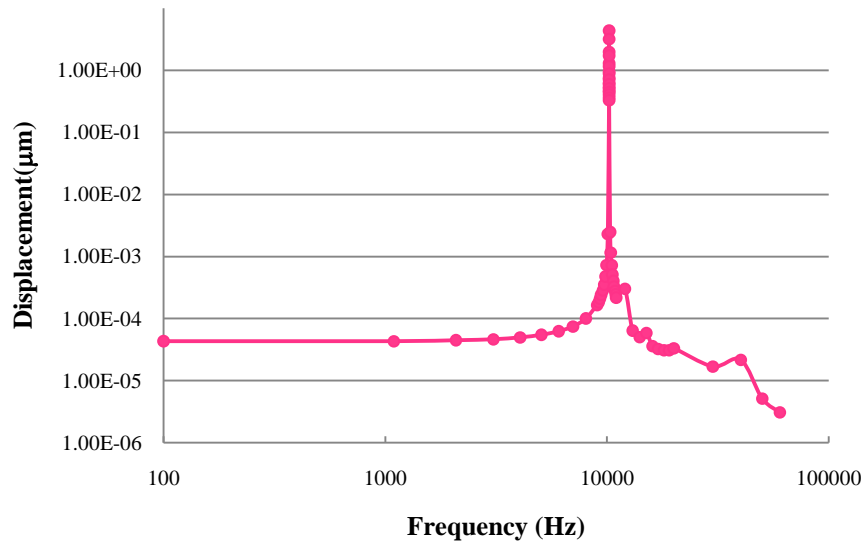Fig. 4.3 Deformation of the structure at resonance

Fig. 4.4 Harmonic response of the finite element model

4.1.2 Simulation

The Simulink model of the open-loop system is shown in Fig. 4.5 with the "Plant" block shown as Fig. 4.1 The "Omega_in" block is a step input at $t = 0.1\text{sec}$ with a step value of 1.745. Fig. 4.6 shows the simulation result of the drive force on the drive axis. The left part is for $0 < t < 2\,\text{sec}$ and the right part is for $0.0995\,\text{sec} < t < 0.1005\,\text{sec}$. The same apply to the other time domain simulation results in the following. Fig. 4.7 shows the simulation result of the Coriolis force produced by the drive axis on the sense axis. Fig. 4.8 shows the displacement of the drive axis. The Coriolis force produced by the sense axis on the drive axis is $2m\Omega\dot{y} = 6.84 \times 10^{-9}\cos(64214t)\,\text{N}$, which is much smaller than the drive force. Therefore, the Coriolis force produced by the sense axis almost has no effect on the drive axis. Fig. 4.9 shows the simulation result of the displacement of the sense axis. Without a controller, the settling time is 64 ms. However, the responses of the two axes have no overshoot.
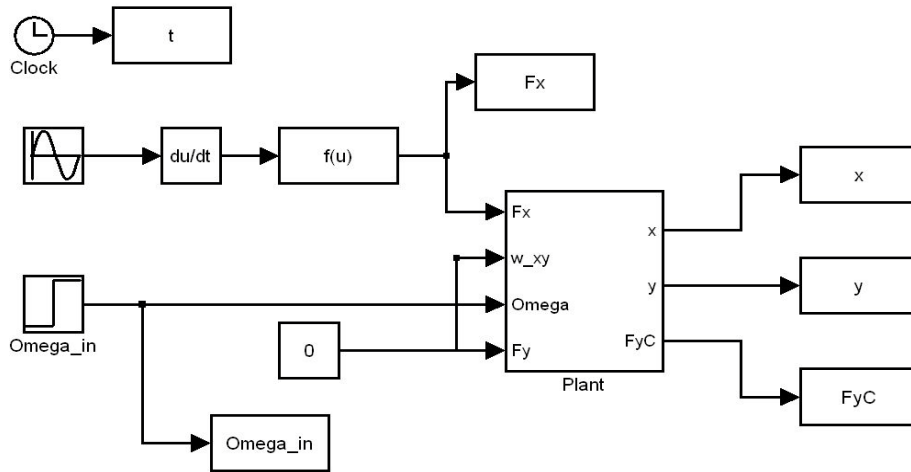
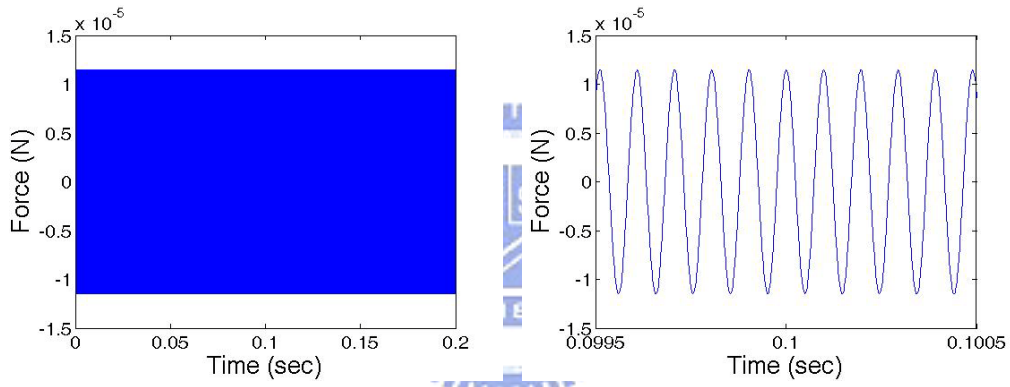Fig. 4.5 Simulink model of the open-loop system

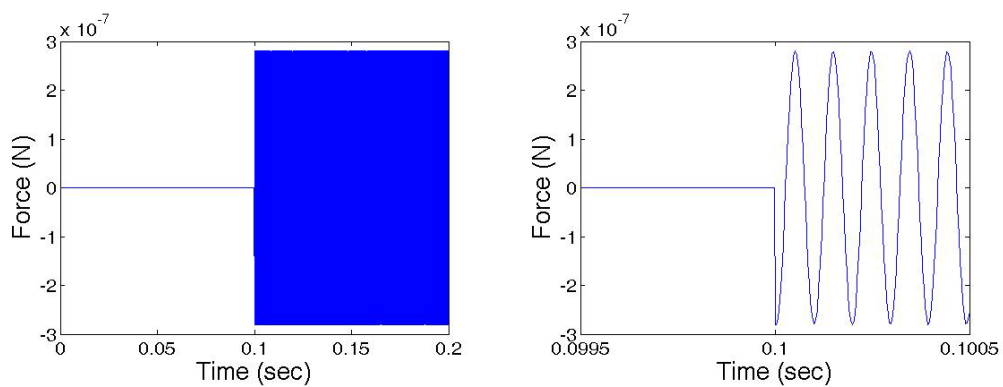Fig. 4.6 Input force on the drive axis in the open-loop system

Fig. 4.7 Coriolis force from the drive axis on the sense axis in the open-loop system
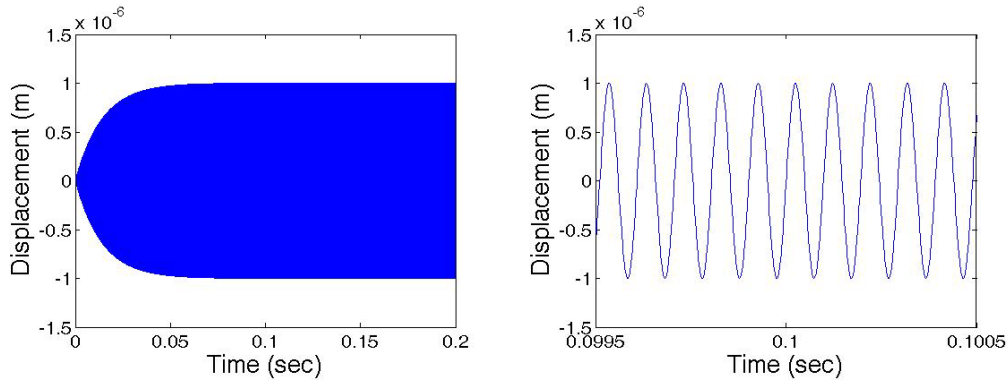
Fig. 4.8 Displacement of the drive axis in the open-loop system
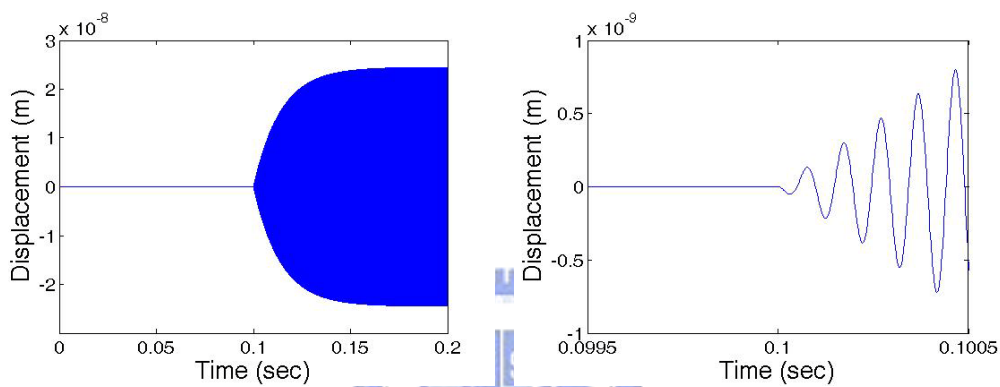
Fig. 4.9 Displacement of the sense axis in the open-loop system

The open-loop response of the system with a quadrature error of $\omega_{xy}^2 = 6421.4 \ \text{rad/sec}$ is shown in Fig. 4.10 and Fig. 4.11. The force produced by quadrature error term is $-m\omega_{xy}^2 x = -8.03 \times 10^{-9} \sin 64214t$ N. The simulation result of the force on the sense axis is shown in Fig. 4.10. The simulation result of the displacement of the sense axis is shown in Fig. 4.11. The response before 0.1sec is caused by the quadrature error. The response after 0.1sec is caused by the Coriolis force and the quadrature error. The calculated and simulated amplitudes of various signals are shown in Table 4.1. The settling time in Fig. 4.8 and Fig. 4.9 is 50ms, which is longer than the specification. The amplitude of the sense axis and the effect of a controller will be compared in the following sections.

47

The Coriolis force on sense axis, $-2m\Omega\dot{x}$, and the quadrature error term, $-m\omega_{xy}^2 x$, can be calculated. It is found that the Coriolis force is 35 times larger than the quadrature error term, therefore the quadrature error can be neglected at $\Omega = 100\,^{\circ}/\sec$.

Fig. 4.10 Force on the sense axis in the open-loop system with quadrature error
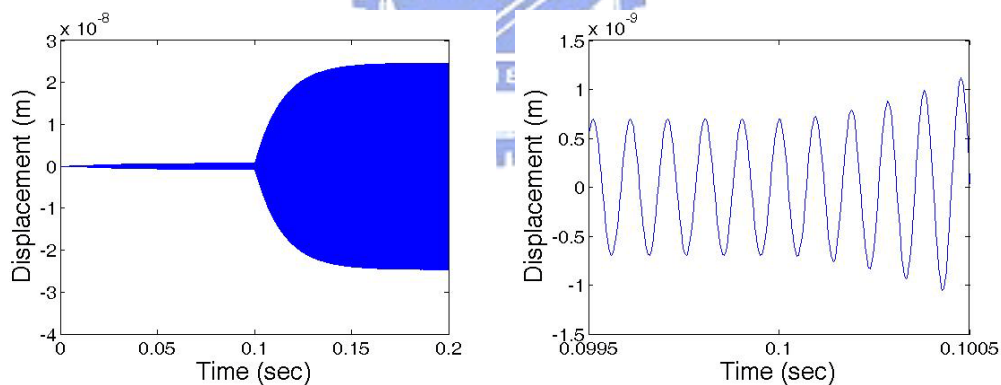
Fig. 4.11 Displacement of the sense axis in the open-loop system with quadrature error
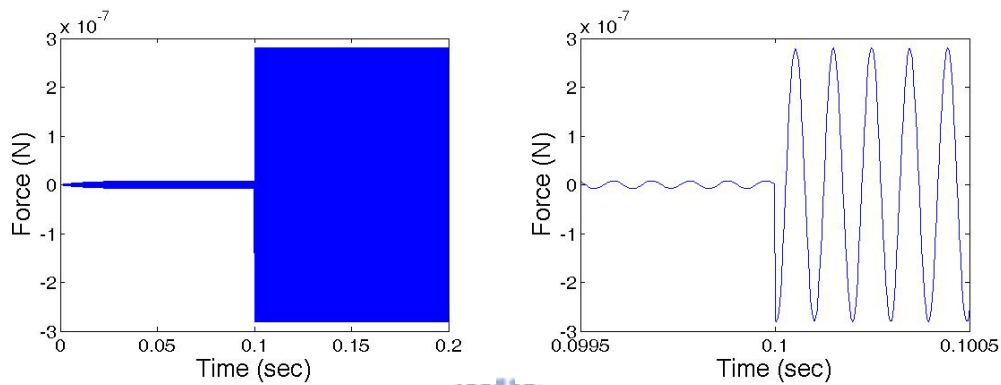
Table 4.1 Calculated and simulated response amplitude of the open-loop system

	Calculations (amplitude)	Simulations (amplitude)	
		Without quadrature error	With quadrature error
F_x (N)	1.15×10^{-5}		
F_y (N)	2.80×10^{-7}	2.80×10^{-7}	2.80×10^{-7}
x (m)	1.00×10^{-6}	1.00×10^{-6}	
y (m)	2.44×10^{-8}	2.46×10^{-8}	2.46×10^{-8}

4.2 PID controller using pole placement

The PID controller designed in section 3.2 is used to control the gyroscope. The Simulink model is shown in Fig. 4.12. In the force balance control loop, the controller output on the sense axis is the feedback force. It is equal to the Coriolis force and proportional to the angular rate. Therefore the controller output is used in the following to discuss its performance.

Fig. 4.12 Simulink model of the closed-loop system with a PID controller

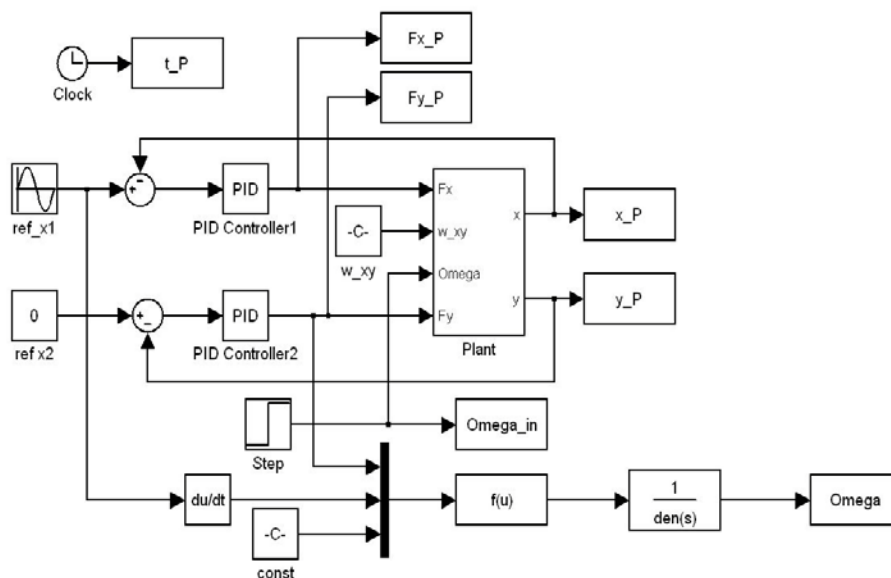Fig. 4.13 and Fig. 4.14 show the simulation results of the controller output on the drive axis and the sense axis. On the drive axis, the amplitude of the closed-loop controller outputs almost equals the one of the open-loop input force. On the sense axis, the closed-loop controller output almost can cancel the open-loop Coriolis force. Fig. 4.15 and Fig. 4.16 show simulation results of the displacements of the two axes. The displacement of the drive axis can be controlled at 1μm amplitude whether the quadrature error exists or not. The displacement of the sense axis can be controlled at 4.924×10^{-11} m, which is much smaller than that in the open-loop system as shown in Fig. 4.11. The effect of the controller is shown in Fig. 4.17 where the angular rate 100°/sec is added to the system at $t = 0.1$sec and the PID controller is turned on at $t = 0.2$sec. From Fig. 4.17, it can be seen that the displacement is reduced from 10^{-8}m to 10^{-11}m in 0.2ms. The demodulated angular rate is shown in Fig. 4.18 with a settling time of 0.7ms. The simulation results are summarized in Table 4.2.
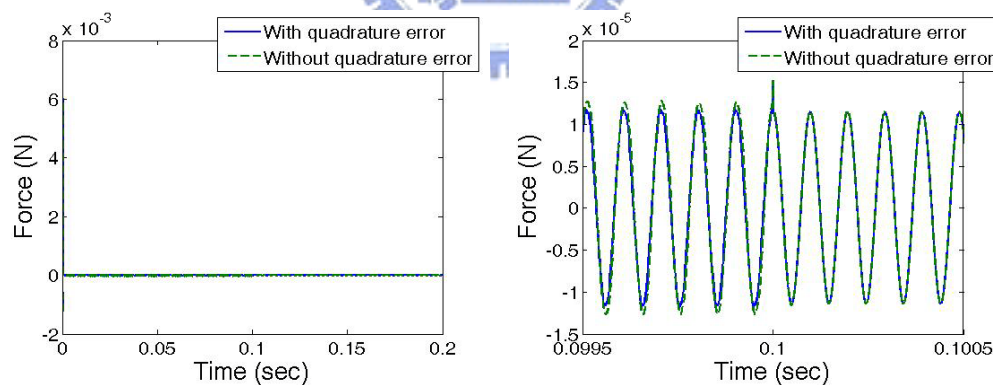

Fig. 4.13 Controller output on the drive axis in the closed-loop system with a PID controller
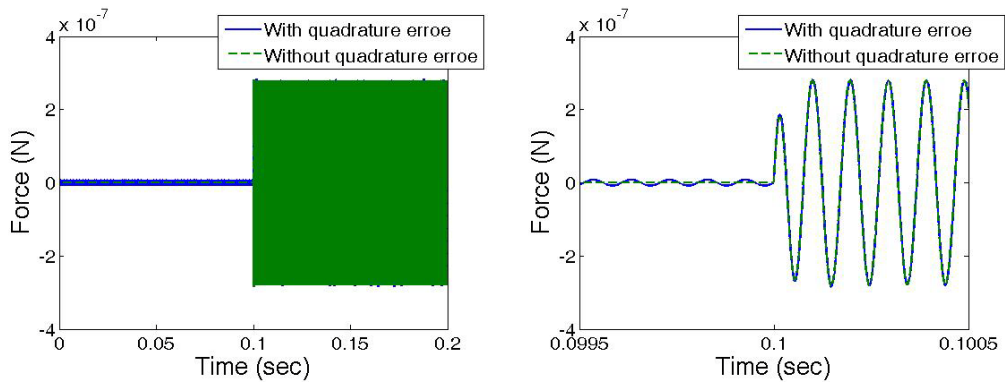
Fig. 4.14 Controller output on the sense axis in the closed-loop system with a PID controller
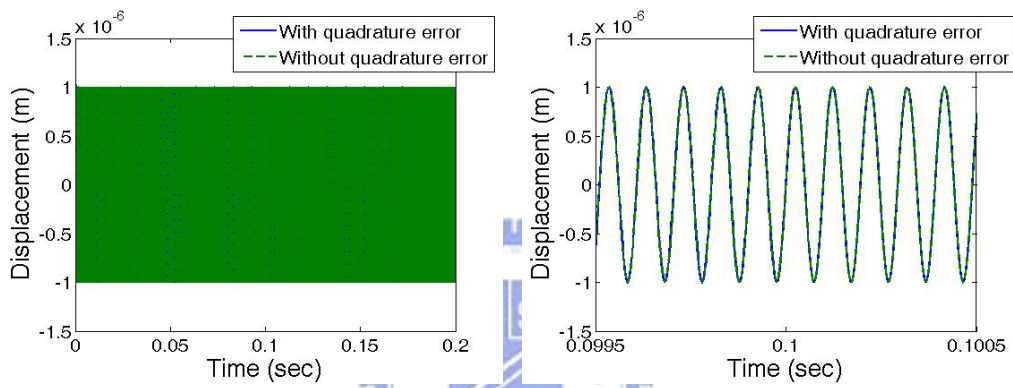
Fig. 4.15 Displacement of the drive axis in the closed-loop system with a PID controller
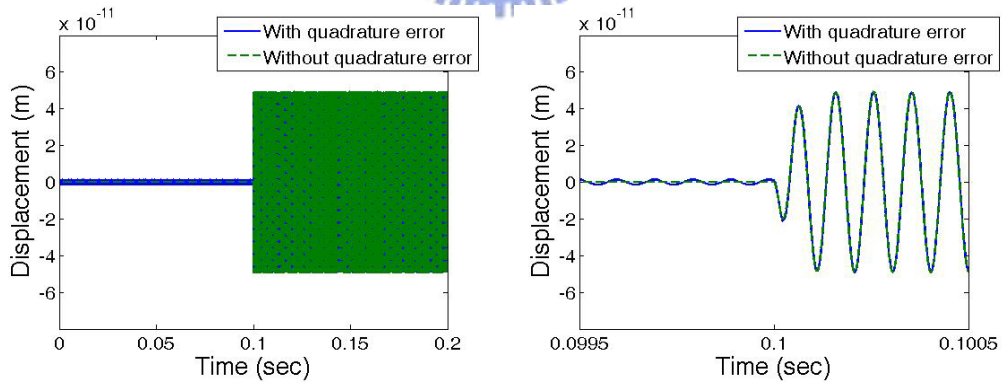
Fig. 4.16 Displacement of the sense axis in the closed-loop system with a PID controller
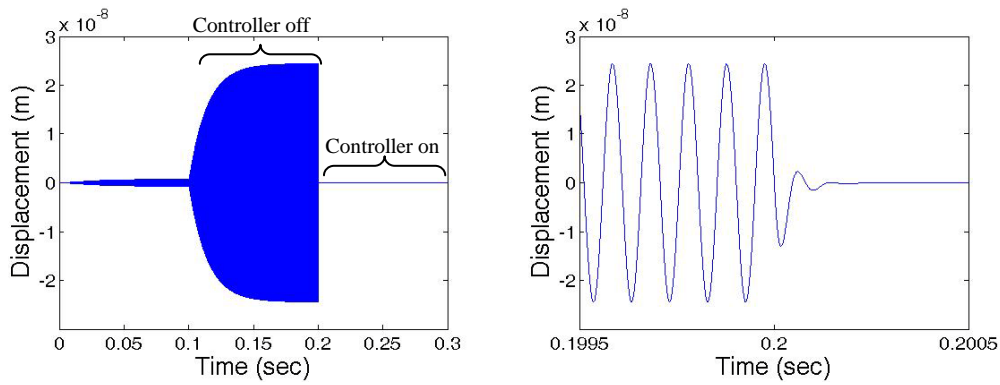
Fig. 4.17 Effect of the PID controller on the displacement of the sense axis
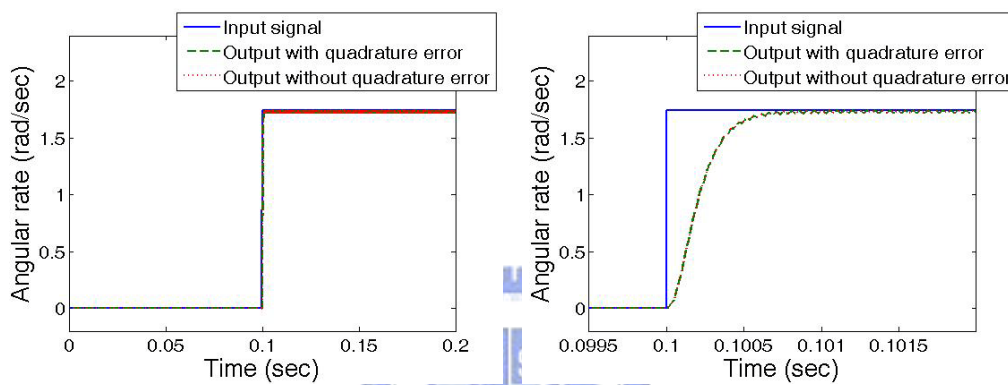
Fig. 4.18 Angular rate of the close-loop system with a PID controller

Table 4.2 Simulation results of the closed-loop system with a PID controller for $\Omega =$ 100°/sec

	Simulations(amplitude)	
	Without quadrature error	With quadrature error
F_x (N)	1.15×10^{-5}	1.15×10^{-5}
F_y (N)	2.80×10^{-7}	2.79×10^{-7}
x (m)	1.00×10^{-6}	1.00×10^{-6}
y (m)	4.92×10^{-11}	4.92×10^{-11}
Demodulated Ω (rad/sec)	1.74	1.73

4.3 QFT/H$_\infty$ control

The Simulink model of the closed-loop system with a QFT/H$_\infty$ controller is

52

shown in Fig. 4.19. The "H_inf controller" block and the "Prefilter" block were discussed and designed in section 3.3 and shown in Eq. 3.19. Compared to Fig. 4.12, the QFT/H$_\infty$ control loop is similar to the PID loop except for the additional prefilter.
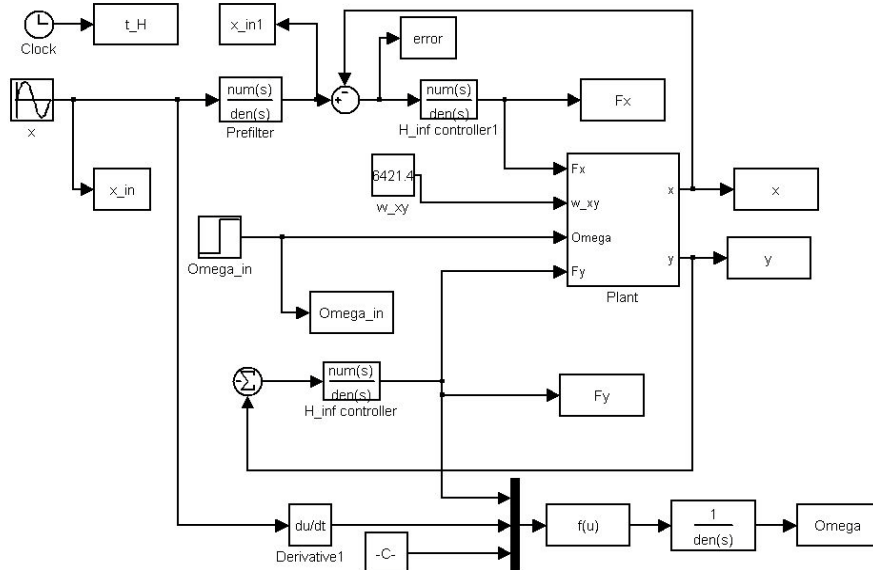
Fig. 4.19 Simulink model of the closed-loop system with a QFT/H$_\infty$ controller

Fig. 4.20 and Fig. 4.21 show the controller outputs F_x and F_y on the drive the sense axes. Fig. 4.22 and Fig. 4.23 show the displacements of the two axes. From Fig. 4.22, it is obvious that the displacement of the drive axis is almost not effected by the Coriolis force from the sense axis and the quadrature error. This is because that the two forces are much smaller than the drive force. From Fig. 4.23, the displacement of the sense axis can be controlled at 7.88×10^{-11} m. The demodulated angular rate is shown in Fig. 4.24. It can be observed that the demodulated angular rate is smaller than the input step value. Even for $t < 0.1\sec$, there is a non-zero output when the input angular rate is zero. But this situation did not happen in the PID controller in the previous section. The difference of the two control loops is the prefilter. If the prefilter is removed temporarily, the force on the sense axis is shown in Fig. 4.25. Obviously

the prefilter causes a response delay. Because the reference input is a harmonic signal at the resonance frequency, the transfer function of the prefilter Eq. 3.19 can be evaluated as:

$$F\left(64214\,j\right) = \frac{6.05 + 3.08\,j}{-1.12 + 7.06\,j} = \frac{e^{0.562\,j}}{e^{1.728\,j}} = e^{-1.166\,j} \tag{4.4}$$

The magnitude of the gain is 1, and the phase is -1.166 rad/sec. In the presence of the system delay caused by the prefilter, the demodulated signal becomes:

$$u_y \cdot \cos(\omega t) = \left(-\omega_{xy}^2 x - 2\Omega \dot{x}\right) \cdot \cos(\omega t), \text{ where } x = A\sin(\omega t + \phi) \tag{4.5}$$
$$\Rightarrow \Omega' = \mathrm{F_{LPF}}\left(-\frac{u_y \cdot \cos(\omega t)}{A\omega}\right) = \Omega\cos\phi + \frac{1}{2}\frac{\omega_{xy}^2}{\omega}\sin\phi, \text{ where } \phi = -1.166.$$

The demodulated output Ω' is different from the input rate Ω if $\phi \neq 0$. With the values of Ω, ω, ϕ, and ω_{xy}^2 discussed above, it is found $\Omega' = -0.046^\circ/\sec$ when $\Omega = 0$ and $\Omega' = 0.64^\circ/\sec$ when $\Omega = 100^\circ/\sec$, which is close to the simulated results.

Since the system works at a single frequency, the prefilter can be removed from this loop to eliminate the system delay. The angular rate without the prefilter in the control loop is shown in Fig. 4.26. The simulation results are summarized in Table 4.3.
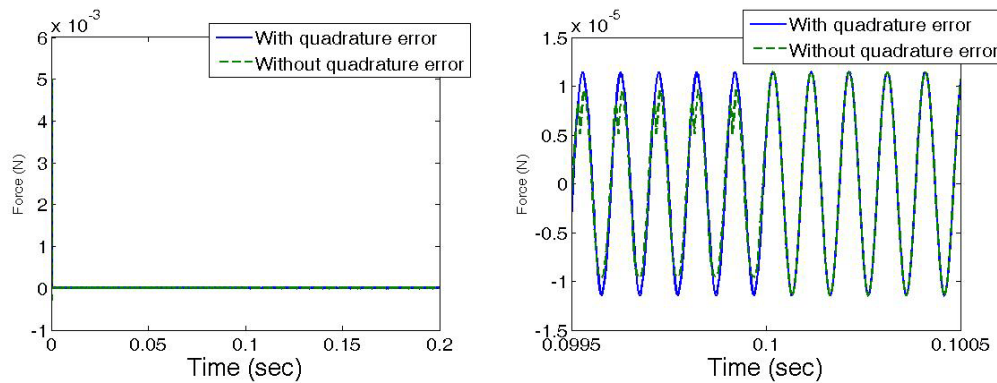
Fig. 4.20 Controller output on the drive axis in the closed-loop system with a QFT/H$_\infty$ controller
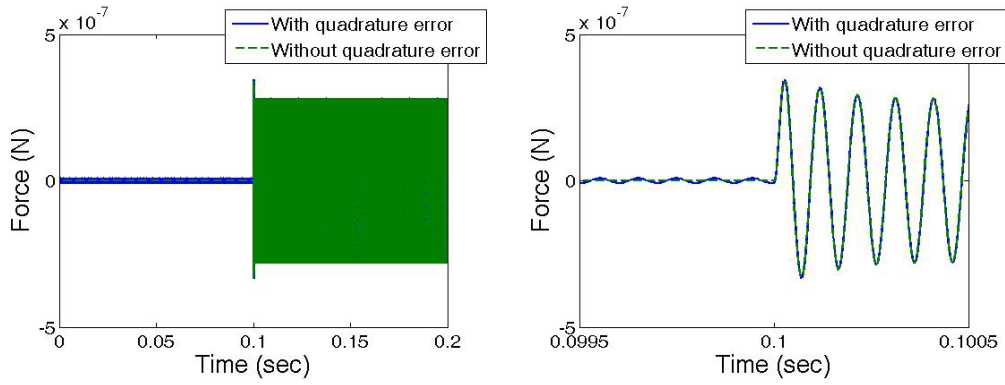
Fig. 4.21 Controller output on the sense axis in the closed-loop system with a QFT/H$_\infty$ controller
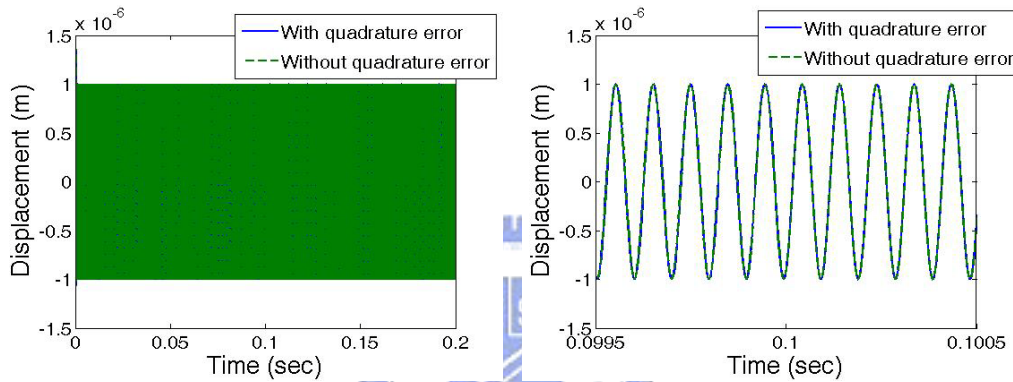
Fig. 4.22 Displacement of the drive axis in the closed-loop system with a QFT/H$_\infty$ controller

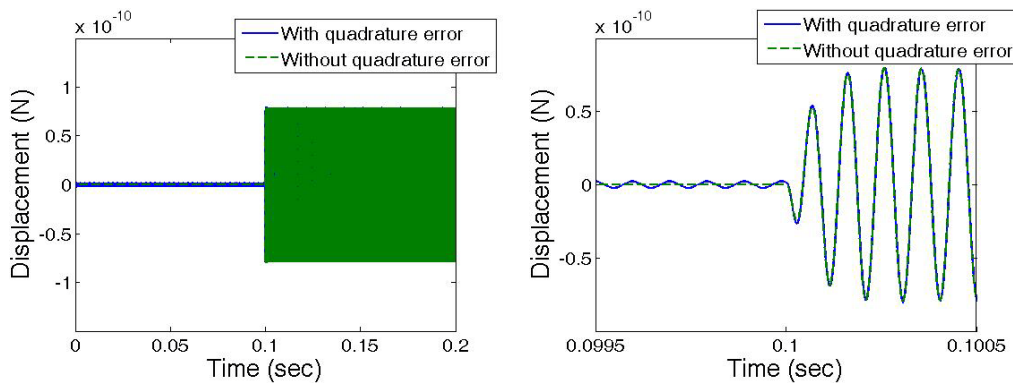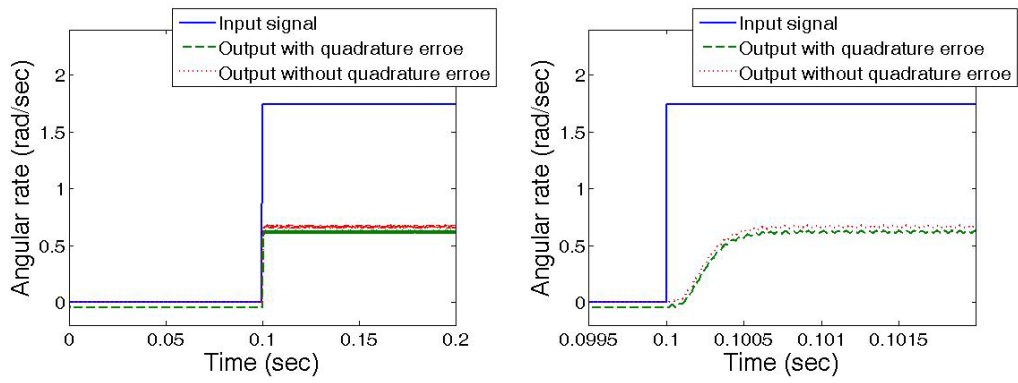Fig. 4.23 Displacement of the sense axis in the closed-loop system with a QFT/H$_\infty$ controller

Fig. 4.24 Angular rate of the close-loop system with a QFT/H$_\infty$ controller
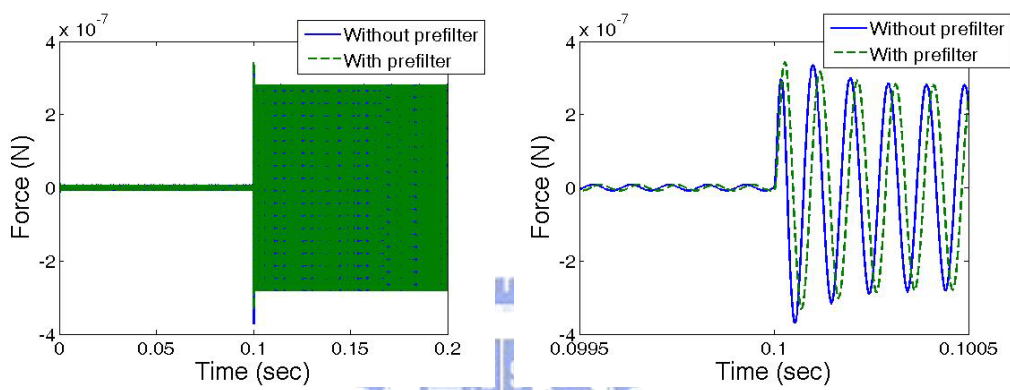

Fig. 4.25 Feedback force of sense axis of close-loop system by QFT/H$_\infty$ control with and without prefilter
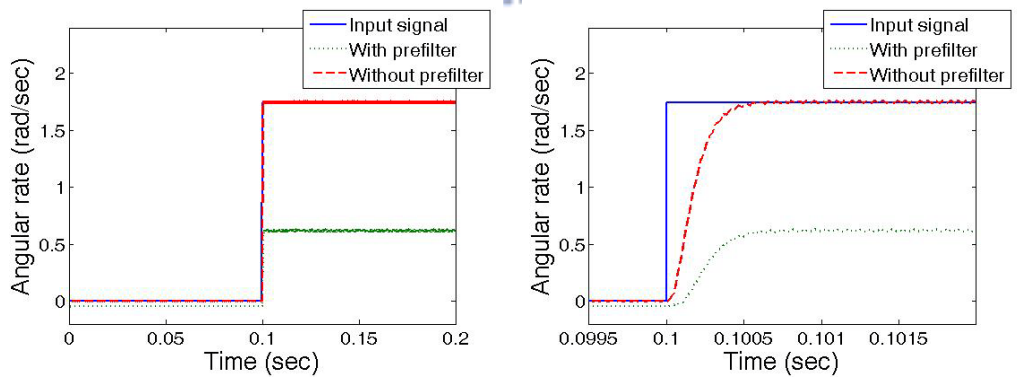
Fig. 4.26 Angular rate of close-loop system by QFT/H$_\infty$ control with and without prefilter

Table 4.3 Simulation results of the closed-loop system with a QFT/H$_\infty$ controller for $\Omega = 100°/sec$

	Simulations(amplitude)	
	Without quadrature error	With quadrature error
F_x (N)	1.15×10^{-5}	1.15×10^{-5}
F_y (N)	2.80×10^{-7}	2.80×10^{-7}
x (m)	1×10^{-6}	1×10^{-6}
y (m)	7.88×10^{-11}	7.88×10^{-11}
Ω with prefilter (rad/sec)	0.67	0.62
Ω without prefilter (rad/sec)	1.75	1.75

4.4 Robustness

In this section, the robustness of the open-loop system, the PID control loop and the QFT/H$_\infty$ control loop are compared. It is assumed that the quadrature error exists, and there are variations in the damping coefficient and the natural frequency. In addition, the feedback forces on the sense axis are discussed to avoid demodulation error. Because the open-loop system does not have feedback control, the action force on the sense axis in the open-loop system should be multiplied by -1 to be compared with controller output on the sense axis in the closed-loop system.

The robustness comparisons of three controllers are shown in Fig. 4.27. Fig. 4.27 (a) shows the simulation results without system variation; Fig. 4.27 (b) is the results with 10% variation in natural frequency; Fig. 4.27 (c) is the results with 10% variation in damping coefficient; Fig. 4.27 (d) is the results with 10% variation in both the natural frequency and damping coefficient. The simulation results are summarized in Table 4.4. It is assumed that the variations of the two axes are the same in this simulation. The first row of Table 4.4 shows the forces without any system variations.

The other rows show the forces and relative errors for various system variations. The relative error is calculated by $\left|(x_0 - x)/x_0\right| \times 100\%$, where x and x_0 are the forces with and without system variations in the same column. As shown in Table 4.4, when there is no variation, the force on the sense axis in the open-loop system is 2.8×10^{-7}N; the one in the close-loop system with a PID controller is 2.79×10^{-7} N; the one in the close-loop system with a QFT/H$_\infty$ controller is 2.8×10^{-7} N.

From Table 4.4, the robustness of QFT/H$_\infty$ controller is better than the PID controller, and the influence of natural frequency is larger than the damping coefficient. From Fig. 4.27, it can be observed that the settling times of the PID control and the QFT/H$_\infty$ control are both smaller than 0.2ms and satisfy the specification for all the variations considered in the simulation.

Unequal variations in the two axes were also simulated. For the system with 10% variation in natural frequency of the sense axis only, the simulation results are summarized in Table 4.5. The relative error of the feedback force on the sense axis is 12.5% for the PID controller and 3.2% for the QFT/H$_\infty$ controller. Therefore, even when there are unequal variations or frequency mismatch between the two axes, the QFT/H$_\infty$ controller still has better performance.

(a)   (b)

(c)   (d)
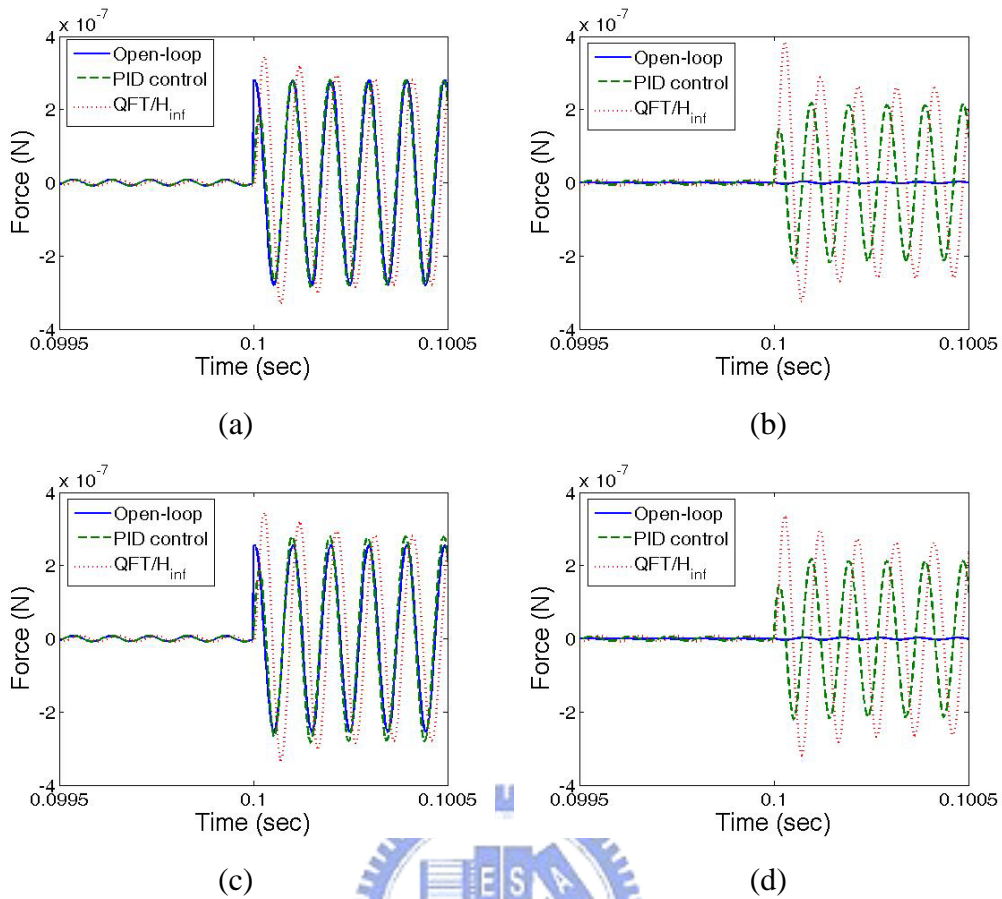
Fig. 4.27 Robustness comparisons of three controllers (a) without system variation, (b) with 10% variation in natural frequency, (c) with 10% variation in damping coefficient, (d) with 10% variation in both the natural frequency and damping coefficient

Table 4.4 Robustness comparison

	Variation (%)		Amplitude of force on the sense axis (N)		
	ω	ξ	Open-loop	PID control	QFT/H$_\infty$ control
1	0	0	$2.80 \times 10^{-7} \, (0\%)$	$2.79 \times 10^{-7} \, (0\%)$	$2.80 \times 10^{-7} \, (0\%)$
2	10	0	$2.76 \times 10^{-9} \, (99\%)$	$2.12 \times 10^{-7} \, (24\%)$	$2.65 \times 10^{-7} \, (5.6\%)$
3	0	10	$2.54 \times 10^{-7} \, (9.2\%)$	$2.80 \times 10^{-7} \, (0.2\%)$	$2.80 \times 10^{-7} \, (0\%)$
4	10	10	$3.15 \times 10^{-9} \, (99\%)$	$2.12 \times 10^{-7} \, (24\%)$	$2.64 \times 10^{-7} \, (5.6\%)$

Table 4.5 Robustness comparison with frequency mismatch

	Variation (%)		Amplitude of force on the sense axis (N)	
	ω_x	ω_y	PID control	QFT/H$_\infty$ control
1	0	0	2.79×10^{-7} (0%)	2.80×10^{-7} (0%)
2	0	10	2.44×10^{-7} (12.5%)	2.71×10^{-7} (3.2%)

4.5 Comparison with other publications

4.5.1 AGC force rebalance control

The QFT/H$_\infty$ control method was compared to the AGC force rebalance control in [16]. The dynamic parameters of the MEMS vibratory gyroscope in [16] are listed in Table 4.6; the block diagram of the system is shown in Fig. 1.8.

Table 4.6 Dynamic parameters of that MEMS vibratory gyroscope in [16]

Resonant frequency $f(\omega)$	7816 Hz (49109 rad/sec)
Mass	3.11×10^{-6} kg
Spring coefficient k	7500 Nm^{-1}
Damping coefficient ξ	0.0014
Amplitude of drive axis	0.32 μm

The QFT/H$_\infty$ control method is used to design the controller for the system in Table 4.6 with the following results:

$$K(s) = \frac{1.395 \times 10^{10}(s+918.3)(s^2+137.6s+2.412 \times 10^9)}{(s+918)(s+9.19 \times 10^{-4})(s^2+5.887 \times 10^5 s+9.023 \times 10^{10})}$$

$$F(s) = \frac{0.4\,(s+2 \times 10^5)}{(s+8 \times 10^4)}$$

(4.6)

The drive mode has an amplitude of 0.32μm at the resonance of 49109 rad/sec. A 0.5 rad/sec angular rate was added to the system at $t = 0.01$ sec. The simulation result by

the QFT/H_∞ controller and AGC force rebalance controller [16] are shown in Fig. 4.28 and Fig. 4.29. Obviously, the transient performance of QFT/H_∞ control is better than the result in [16].
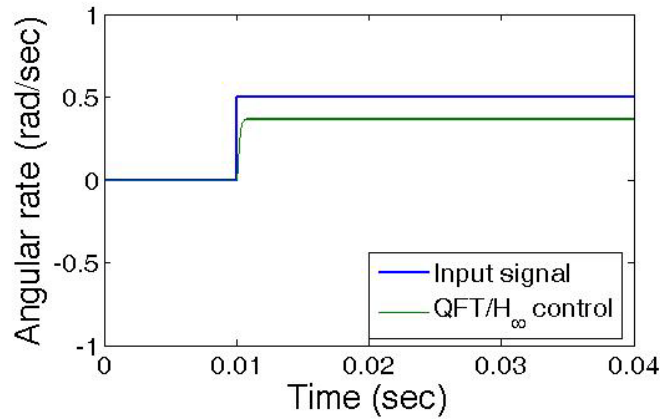
Fig. 4.28 Simulation result with QFT/H_∞ control
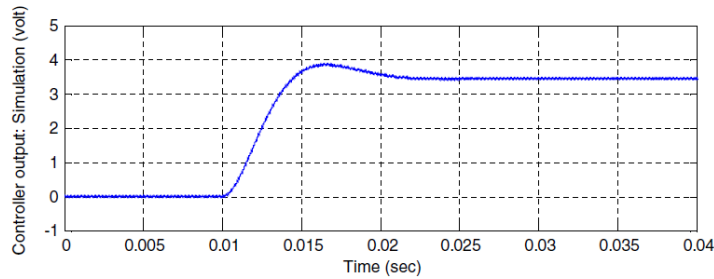
Fig. 4.29 Step response of the simulation results [16]

4.5.2 H_∞ control

The QFT/H_∞ control method is also compared to the H_∞ control method in [4]. The system block diagram of the MEMS gyroscope in [4] is shown in Fig. 1.7. A conventional H_∞ control method is used to design the H_∞ controller. Though the parameters of this plant [4] are different from the plant in this thesis, the equations of motion of the gyroscope are the same. The concept of H_∞ control is applied to both controller designs. Therefore, we can still compare their performance in robustness.

For resonant frequency variation of 2% and 4%, Fig. 4.30 shows that controller output has variation of 0.5% and 2.5%, respectively [4].

Fig. 4.31 is the results with the same resonant frequency variations by QFT/H$_\infty$ control. The variation of the QFT/H$_\infty$ controller is 0.3% and 1.7%, respectively. It can be observed that the robustness and transient performance of QFT/H$_\infty$ control is better than the result in [4]. In addition, the result of the QFT/H$_\infty$ controller and H$_\infty$ controller in [4] are output feedback and state feedback, respectively. In reality, to realize the controller using output feedback is easier than using state feedback. Therefore, the QFT/H$_\infty$ controller can be realized more easily than the H$_\infty$ controller.
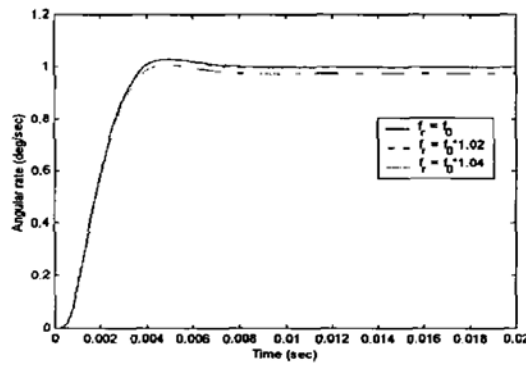
Fig. 4.30 Controller output resonant frequency variation by H$_\infty$ controller in [4]
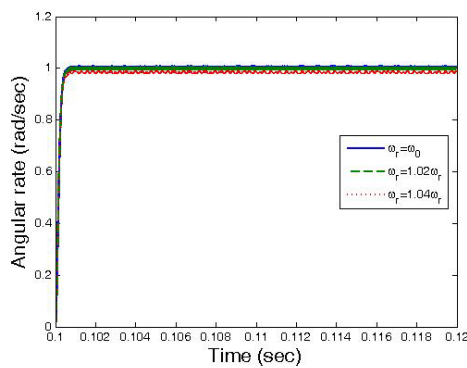
Fig. 4.31 Simulation result with QFT/H$_\infty$ control

4.6 Summary

In this chapter, the QFT/H_∞ control method was compared to the PID control and other control methods. Both PID control and QFT/H_∞ control have good performance. The amplitude of the sense axis in the open-loop system is reduced from 10^{-8}m to 10^{-11}m by using a PID controller or a QFT/H_∞ controller. When there is a 10% variation in the system, the variation of response with a PID controller is 24%, and the variation of response with a QFT/H_∞ controller is just 5.6%. Thus, the QFT/H_∞ control has better robustness.

Chapter 5   Conclusion and Future Work

5.1 Conclusion

In this thesis, the PID controller and the QFT/H_∞ controller are applied to the MEMS vibrating gyroscope. The amplitude of drive axis can be maintained at 1μm, and the amplitude of sense axis can be maintained at less than 10^{-4}μm for both PID control and QFT/H_∞ control. The performance of different control methods are simulated and discussed. When the natural frequency and the damping coefficient both have the variation of 10%, the variations of the response using QFT/H_∞ and PID control are 5.6% and 24%, respectively. Therefore, the QFT/H_∞ control method has better robustness when the fabrication errors and the model uncertainties exist. In addition, the transient performance of this control method is better than the AGC force rebalance control in [16]. The variations of the response of the QFT/H_∞ control and the H_∞ control in [4] are 1.7% and 2.5%, respectively. The robustness and transient performance of the QFT/H_∞ control are better. Since the reference signal is at single frequency, the prefilter in the QFT/H_∞ controller can be removed to eliminate the system delay and erroneous demodulation. In such a case, the loop becomes an output feedback loop, which is easier for realization compared to the conventional H_∞ control which is a state feedback loop.

5.2 Future work

The transfer function of the QFT/H_∞ controller is a 4th-order function. For realization, to reduce the order of the function to 3rd-order even 2nd-order may be required. In this thesis, the angular rate is 100°/sec and the Coriolis force is 35 times larger than the quadrature error term. In the future, it is necessary to consider the

effect on the system response caused by the quadrature error term when the angular rate is smaller. Besides, the effect on the system robustness caused by the structure asymmetry of the two axes when $m_x \neq m_y$ should be considered.

References

[1]   V. P. Veiko, "Laser-assisted microshaping," in *Laser-Assisted Microtechnol*, 2001, pp. 93-104.

[2]   S. Park, R. Horowitz, and C.-W. Tan, "Adaptive control for MEMS gyroscopes," *California Partners for Advanced Transit and Highways (PATH)*, 2002.

[3]   D. Lili, "Adaptive control system for a vibrational MEMS gyroscope with time-varying rotation rates," *Ph.D. dissertation, University of Alabama*, 2005.

[4]   S. Woon-Tahk, L. Jang Gyu, S. Jin Woo, and K. Taesam, "H∞ controller design of MEMS gyroscope and its performance test," in *Position Location and Navigation Symposium, 2004. PLANS 2004*, 2004, pp. 63-69.

[5]   Z. Qing, D. Lili, and G. Zhiqiang, "Control and rotation rate estimation of vibrational MEMS gyroscopes," in *Control Applications, 2007. CCA 2007. IEEE International Conference on*, 2007, pp. 118-123.

[6]   C. Acar, "Robust micromachined vibratory gyroscopes," *Ph.D. dissertation*, *University of California*, 2004.

[7]   H. Ueno, M. Hosaka, Y. Zhang, O. Tabata, S. Konishi, and S. Sugiyama, "Study on fabrication of high aspect ratio microparts using the LIGA process," in *Micromechatronics and Human Science, 1997. Proceedings of the 1997 International Symposium on*, 1997, pp. 49-54.

[8]   N. Mengnian, X. Weichen, W. Xiaodong, X. Jianfang, Y. Genqing, and W. Weiyuan, "Design and characteristics of two-gimbals micro-gyroscopes fabricated with quasi-LIGA process," in *Solid State Sensors and Actuators, 1997. TRANSDUCERS '97 Chicago*, 1997, pp. 891-894.

[9]   X. Huikai and G. K. Fedder, "A CMOS-MEMS lateral-axis gyroscope," in *Micro Electro Mechanical Systems, 2001. MEMS 2001. The 14th IEEE International Conference on*, 2001, pp. 162-165.

[10] K. Maenaka, Y. Konishi, T. Fujita, and M. Maeda, "Analysis and design concept of highly sensitive silicon syroscope," in *Solid-State Sensors and Actuators, 1995 and Eurosensors IX.. Transducers '95. The 8th International Conference on*, 1995, pp. 612-615.

[11] A. Sharma, F. M. Zaman, B. V. Amini, and F. Ayazi, "A high-Q in-plane SOI tuning fork gyroscope," in *Sensors, 2004. Proceedings of IEEE*, 2004, pp. 467-470.

[12] F. Ayazi and K. Najafi, "A HARPSS polysilicon vibrating ring gyroscope," *Journal of Microelectromechanical Systems,* vol. 10, pp. 169-179, 2001.

[13] M. Palaniapan, R. T. Howe, and J. Yasaitis, "Performance comparison of integrated z-axis frame microgyroscopes," in *Micro Electro Mechanical Systems, 2003. MEMS-03 Kyoto. IEEE The Sixteenth Annual International Conference on*, 2003, pp. 482-485.

[14] P. Sungsu and R. Horowitz, "Adaptive control for the conventional mode of operation of MEMS gyroscopes," *Journal of Microelectromechanical Systems,* vol. 12, pp. 101-108, 2003.

[15] R. Oboe, R. Antonello, E. Lasalandra, G. S. Durante, and L. Prandi, "Control of a Z-axis MEMS vibrational gyroscope," *Mechatronics, IEEE/ASME Transactions on,* vol. 10, pp. 364-370, 2005.

[16] S. Woon-Tahk, S. Sangkyung, L. Jang Gyu, and K. Taesam, "Design and performance test of a MEMS vibratory gyroscope with a novel AGC force rebalance control," *Journal of Micromechanics and Microengineering,* vol. 17, pp. 1939-1948, 2007.

[17] M. J. Sidi, "A combined QFT/H design technique for TDOF uncertain feedback systems," *International Journal of Control,* vol. 75, pp. 475-489, 2002.

[18] N. Yazdi, F. Ayazi, and K. Najafi, "Micromachined inertial sensors," *Proceedings of the IEEE,* vol. 86, pp. 1640-1659, 1998.

[19] G. F. Franklin, J. D. Powell, and E. N. Abbas, *Feedback control of dynamic systems*, 3 ed.: Addison Wesley, 1994.

[20] J.-H. Kim and K.-K. Choi, "Design of direct pole placement PID self-tuners," *Industrial Electronics, IEEE Transactions on,* vol. IE-34, pp. 351-356, 1987.

[21] I. M. Horowitz and M. Sidi, "Synthesis of feedback systems with large plant ignorance for prescribed time-domain," *International Journal of Control,* pp. 287 - 309, 1972.

[22] K. Zhou and J. C. Doyle, *Essentials of robust control*: *Prentice Hall*, 1999.

[23] K. Zhou, J. C. Doyle, and K. Glover, *Robust and optimal control*: *Prentice Hall*, 1998.